Dynamic behavior of concrete and cementitious materials

Ezio Cadoni, Pascal Forquin

Chapter 15 - Dynamic behaviour of concrete and cementitious materials

Ezio Cadoni [1], Pascal Forquin [2]
[1] *University of Applied Sciences and Arts of Southern Switzerland, DynaMat SUPSI Lab, Mendrisio, Switzerland*
[2] *University Grenoble Alpes, CNRS, G-INP, 3SR Lab., Grenoble, France*

Abstract

Understanding the dynamic response of concrete and cement-based materials is essential for designing structures that can withstand intense loading conditions, including civil, defense, and critical infrastructures. This chapter provides a comprehensive review of the latest advancements in the mechanical characterization of concrete and cementitious materials under dynamic loading. It focuses on understanding the fracture behavior exhibited by these materials and discusses the challenges encountered during high strain rate testing. By gaining insights into the dynamic behavior of these materials, engineers and researchers can enhance their ability to develop resilient and robust structures capable of withstanding extreme loading conditions.

15.1 Introduction

Nowadays, cementitious materials are the most widely used building materials. The construction industry relies heavily on concrete and specialty mortar products because they are adaptable to all forms, possess good mechanical properties, are reasonably priced and readily available. This is evidenced by their massive use. In fact, 4 billion tons of cement and 9-13 billion cubic meters (21-30 billion tons) of concrete are produced annually. Since the 1960s, thanks to research and market pressure, many improvements have been made enabling the development of modern cement-based materials by using novel chemical admixtures, and binding added materials (silica fume and flying ash). New concrete mixtures with designed workability (self-compacting concrete) adapting their rheology to the moulding needs imposed by the structure form were obtained as well as concrete with a low water/cement ratio, low porosity, and high strength and durability. In the last decades, by introducing macro and micro-fibre (metallic or plastic) new cementitious materials have been developed named fibre-reinforced cementitious composite, or more generally fibre-reinforced concrete. Concretes from the 20th century had an average compressive strength of 20-30 MPa. Today, thanks to Ultra High-Performance Concretes, it is possible to reach 150-200 MPa. The flexibility and adaptability of concrete and cementitious materials make them ideal for the use in the construction industry when it comes to constructing structures (ranging from a single house to a skyscraper) and infrastructures (bridges, dams, roads, etc.). During their lifetime these structures can be subjected to dynamic loading caused by soft and hard impact, explosion, and blast. The mechanical properties of cementitious materials are regularly analysed by standardised procedure and any novelty are consequently investigated by following the same procedures. Due to the lack of standards the dynamic behaviour of cementitious materials is studied by means of several experimental set-ups characterized by impacting elements or mechanisms generating stress-waves. In this chapter, a short overview of the typical set-ups normally adopted for studying concrete and mortar response at different velocities and their advances will be presented.

15.2 Concrete fracture

Concrete is made up of two phases: aggregate and matrix. From a mechanical point of view, the aggregates constitute the load-bearing skeleton and the matrix has the task of holding them together. The aggregates, whether of alluvial origin or produced by crushing, are the most resistant phase. In fact, the rocks from which they originate are usually compact rocks with high strength. Generally, they do not cause problems of lack of strength if they are well matched in grain size and cleaned before mixing. In the absence of this latter condition, the bond between matrix and aggregate may be seriously compromised. In contrast, cement matrix is the most susceptible to factors that negatively affect strength and durability (porosity, residual water content, micro-voids, etc.).

Concrete fracture processes change as a function of the loading rate. The cracking evolution differs significantly when a quasi-static or dynamic load is applied. In the first case, cracks nucleate at weak points such as the interface between aggregate and cementitious matrix (transition zone in Fig. 15.1), voids, or existing microcracks. This cracking can easily propagate because it has enough time to choose and develop along the path of least energy requirements. The extension of microcracks into other areas of higher strength is rather limited because of the low stress level and relaxation of the material. In contrast, under impact loading conditions much energy is introduced into the materials and/or structure in a short time. Therefore, cracks as stress concentration points are forced to develop also along shorter paths characterised by higher resistance such as through stronger matrix zones or through aggregates. Additionally, the rapidly increasing overall stress within such a limited period of time causes extensive microcracking in other areas that can lead to a diffuse cracking process. As a result, strength and deformation capacities are improved. When crack patterns are analysed in these cases, two types of fracture can be identified: interfacial and transgranular fractures (see Fig. 15.1). As far as loading regimes are concerned, the first is dominant in quasi-static conditions, while the second is dominant in impact conditions. In fact, during dynamic tests, a large amount of energy is at disposal, allowing cracks to develop at many weak points

(micro-cracks, voids, interfaces where bleeding weaken the transition zone). Once cracks have begun, they grow in a particular direction even through aggregates and in higher strength zones. This is called transgranular fracture (Fig. 15.1 blue lines). Consequently, cracking patterns are determined by aggregate in terms of size, aspect ratio, orientation, and mechanical properties, as well as placement and proportion.

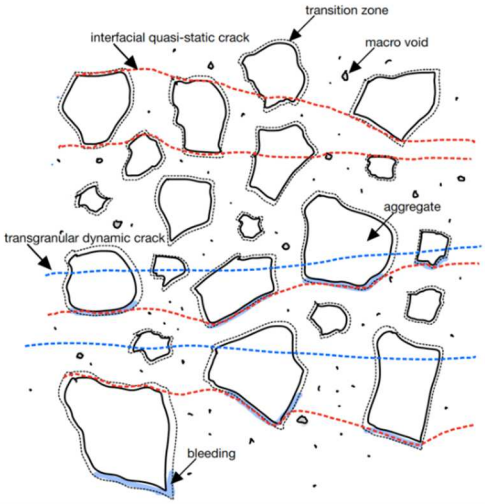

Figure 15.1 – Cracking pattern in quasi-static and dynamic regimes.

According to Figure 15.2a, a plain concrete sample subjected to a quasi-static tensile test reveals that interfacial fractures are the most common failure modes, whereas transgranular fractures are rare. Because of grain boundaries, the fracture surface exhibits rough and irregular characteristics (Fig. 15.2b). While some interfacial cracks persist on the fracture surface under dynamic loadings and the fracture is smoother, transgranular cracks become the dominant failure mode in the last case (Fig. 15.2c).

a) b) c)

Figure 15.2 – Cracking pattern in quasi-static and dynamic regimes: a) quasi-static test; b) quasi-static fracture; c) dynamic fracture.

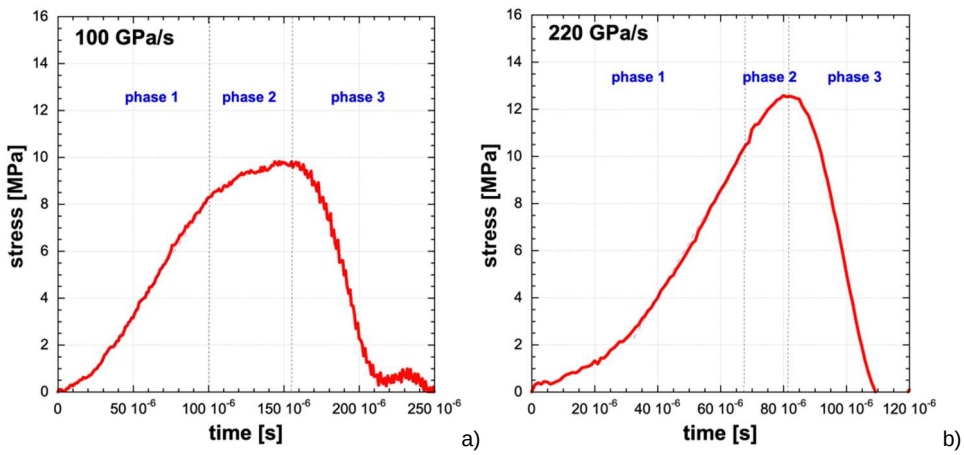

a) b)

Figure 15.3 – Stress vs time of concrete in tension or compression

Concrete specimen can be characterized dynamically by observing both stress vs time (or displacement) curves, as shown in Figure 15.3, where three main branches can be distinguished:

1. a linearly increasing branch that exhibits elastic properties, as represented by its elastic modulus and elastic limit.
2. a strain hardening branch, in which stress increases nonlinearly as strain increases up to the failure strength and,
3. a softening branch, in which decreases load non-linearly as displacement is increased, corresponds to fracture propagation in the specimen cross-section.

The three branches have to be measured using a unique dynamic testing device at high strain rates up to the complete fracture of the specimen. In high strain rate tests, the first branch cannot be unfortunately measured with enough precision because of the lack of equilibrium in the first instants. Split Hopkinson Bars are well-suited to handle the problem of stress wave propagation associated with high strain rate testing. Through numerous stress wave reflections inside the specimen, it can obtain and control homogeneous stress distribution along the specimen gauge length. Non-linear deformation phases 2) and 3) are characterized by displacements and loads of same order of magnitude, so this method assures high measurement accuracy. In contrast, branch 1) of the dynamic stress-strain curve (the elastic one up to the elastic limit) cannot (typically) be accurately determined using the above procedure due to two main reasons:

i) displacement measurements during linear branch 1) are two orders of magnitude smaller than those during non-linear branches 2) and 3), requiring specialized instrumentation;
ii) especially at high loading rates, the time to reach the elastic limit is very short and can cause problems in defining material properties due to non-homogeneous stress distribution across the specimen gauge length.

In the following paragraphs, advances concerning some application proposals for the mechanical characterisation of concrete and cementitious materials in dynamics will be presented.

15.3 Study of the concrete cracking processes

When using standard Hopkinson Bar devices to characterize concrete at high strain rates, a limitation with the material's representativity is encountered. In fact, the actual dimension of the aggregate size is ranging 0-16mm and 0-32mm or larger for special infrastructures such as dams (>50mm). According to a well-known rule of thumb, the size of the concrete sample should be three or four times the maximum size of the aggregate. Hence, a specimen of 100mm size is required for concrete with a maximum aggregate size of 25mm. Additionally, large specimen dimensions required a large diameter Split Hopkinson Bar, which meant that wave dispersion and technical issues became important. To solve these problems, a special equipment named Hopkinson Bar Bundle system (HBB) was developed in the mid-1990s at the Joint Research Center in Ispra and installed in the large dynamic testing facility, which is still present at the European centre today. The HBB is a device that allows precise measurement of the stress-strain diagram, including the softening branch, which is essential for the estimation of the energy absorption capacity of real plain concrete used in civil engineering structures. Referring to Fig. 15.4, the HBB system consists of two bundles of 25 aluminium square bars 40mm side (5 and 7) to which a cubic 200mm side sample (6) is glued by means of an epoxy resin. The bar bundles were constructed from two aluminium prismatic bars with a length of 2 m and a cross section of 200 mm. They were divided into 25 symmetrical pairs of parallel bars by means of the Wire Electro-Discharge Machining process; the remaining 1m remains solid (4 and 8). By instrumenting each bar in the bundle with strain gauges, measurements are made of the incident, reflected, and transmitted pulses acting on each portion of the cross section of concrete specimens facing each of the symmetrical pairs of bars in the bundle by testing concrete specimens with square cross sections of 200mm side. The wave dispersion phenomenon is dramatically reduced, despite the large specimen size. As each elementary bar size in the bundle is small (40mm side), wave dispersion is practically eliminated. In addition to that, it is possible to analyze the kinetics of damage, by comparing the data that each strain gauge provides, to determine the consistency of the damage.

In order to measure incident, reflected, and transmitted pulses acting on the entire cross section of the specimen, the solid portions of the bars as a whole are also equipped with strain gauges. The mechanical pulse is generated by the sudden release of energy stored in 32 high-tensile steel cables (2) 100m in length pulled by a hydraulic jack (1) with a maximum load of 2MN. This pretension is resisted by a grounded explosive bolt in the blocking device (3). Due to an explosive charge, the bolt fails abruptly, causing a tensile mechanical pulse of 40ms duration and linear loading rate to propagate along the Hopkinson bar bundle and cause the concrete sample to fracture. The strain gauge stations on the incident solid bar and incident bar bundle measure incident pulses and reflected pulses. To measure the transmission of pulses through the specimen, strain gauge stations are installed on the transmitted solid bar and transmitted bar bundle.

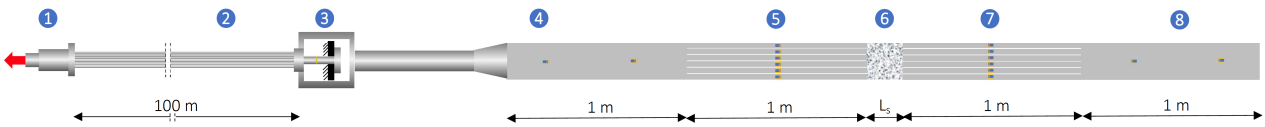

Fig. 15.4 – HBB experimental set-up: 1. hydraulic actuator; 2. high strength steel cables for energy storage; 3. explosive bolt; 4. instrumented input solid aluminium bar; 5. elementary input bar bundle; 6. specimen 7. elementary input bar bundle; 8. instrumented input solid aluminium bar. [Cadoni et al, 2001; 2006]

As can be seen from the literature, the mechanical properties of concrete are strain-rate dependent, so its strength increases at higher loading rates. This is due in part to the fracture process: in the static case, cracks follow the weaker aggregate-mortar interface, while in the dynamic case, cracks propagate through hard aggregates as well. A second aspect is that in the dynamic case, there is usually not just one crack present; often, multiple cracks are active. Therefore, local analysis of the specimen is essential, and the HBB technique provides a solution to this need.

Each of the Nth pairs of specular bars in the two bundles, which have individually instrumented strain gauges, measures only the incident, reflected and transmitted pulses ε_{In}, ε_{Rn}, and ε_{Tn} in the portion of the specimen cross section facing the cross sections of this particular pair during the fracturing process. In Figure 15.5 are sketched the input (a) and output (b) raw signals of the elementary bars of the bundle. The sum of the load measured in the elementary bars is compared with the load measured in the output whole bar are represented in Figure 15.6 for 10 s^{-1} (a) and 1 s^{-1} (b), respectively.

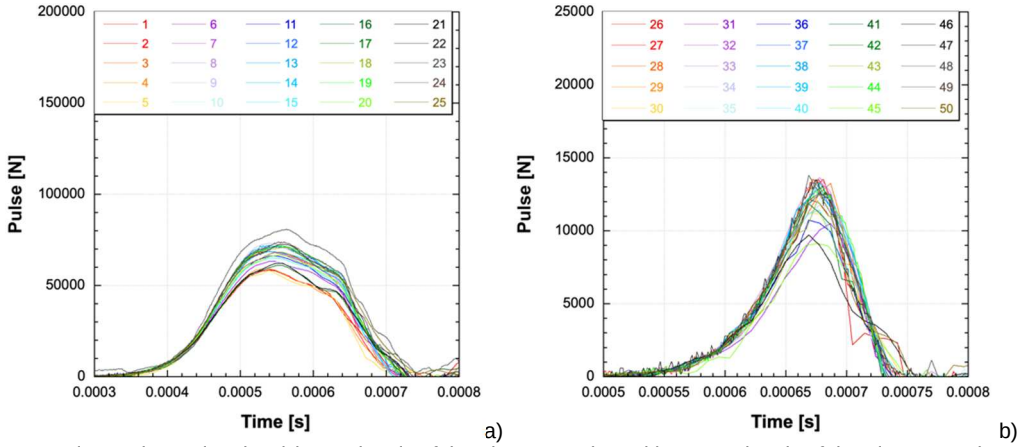

Fig. 15.5 – HBB experimental raw signals: a) input signals of the elementary bars; b) output signals of the elementary bars.

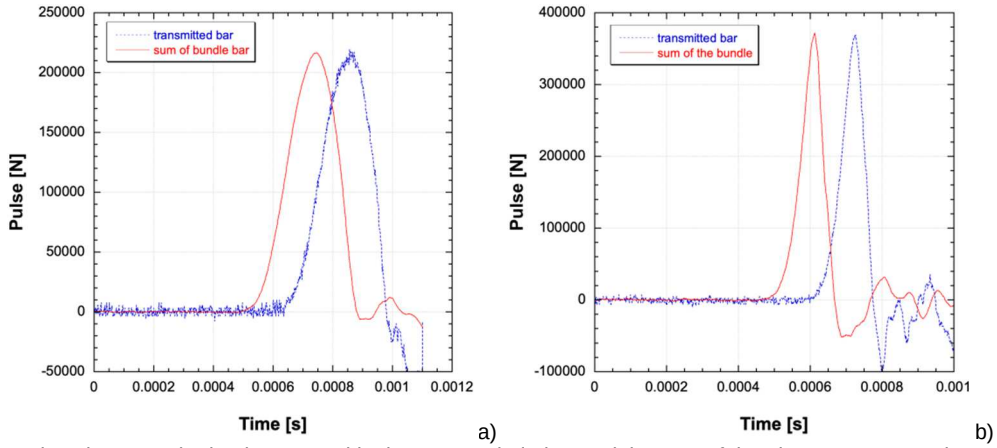

Fig. 15.6 – Comparison between the load measured in the output whole bar and the sum of the elementary output bars of the bundle at 10 s^{-1} (a) and 1 s^{-1} (b).

Each pair of the specular bars of the bundles is assumed to be in one of the following physical states during the fracturing process:

- Observing an uncracked portion of the specimen cross-section, resulting in a relatively small reflected pulse ε_{RN} and a large transmitted pulse ε_{Tn}.
- When facing a semi-cracked cross-section of the specimen, therefore when ε_{RN} is strongly increasing and ε_{TN} is strongly decreasing during measurements
- A totally cracked piece of specimen cross-section is assessed by measuring a reflected pulse ε_{Rn} of equal amplitude and opposite sign to the incident pulse ε_{In}, while the correlated transmitted pulse declines to zero.

The last observations can be used to refine the analysis method for the construction of the true stress-strain diagram based on the bar bundle records. By decreasing the initial value A_0 by an amount corresponding to the separation caused by crack propagation, this refined method presents the residual resisting cross-section A_{TRUE} for each elementary bundle bar on the Nth facing part of the concrete specimen. Fracture mechanics is commonly used to describe concrete cracking under tensile loads. Tensile behaviour can be represented by different phases. Firstly, it is important to remember that micro-damage occurs due to shrinkage of the matrix restrained by the aggregate in the material. Since micro-cracks are randomly distributed, all volume elements have the same probability of having them. In response to increased stress, micro-cracks grow and crack localization takes place, forming macro-cracks. Finally, macro-cracks propagate and the specimen fails.

It is essential to consider the effects of stress wave propagation on cracking processes when the strain-rate is increased from 1 s^{-1} to 10 s^{-1}; in fact, in the static case the crack selects the path with the minimum amount of energy required (i.e. matrix-aggregate interfaces), whereas in the dynamic case wave propagation causes cracking in tougher aggregates as well. A cross-section of the specimen can be used to describe the fracture mode and growth based on the information obtained from the bundle bar. As cracks propagate along a cross-section of the specimen, iso-chrono curves indicate their positions at successive times. Figures 15.7a and 15.7b show crack propagation for two tests at 10 and 1 s^{-1}, respectively, along with the iso-chrono curves of the crack positions during fracture. As it can be seen in Fig. 15.7a, there is no unique crack beginning and growing from a single point, but several macro-cracks which are propagating simultaneously from many points; in other words, multi-activation of cracks is evident. Fig. 15.7a shows that the crack initiation spreads all over the cross-section of the specimen in the very short time of about 20μs, supporting the multi-activation of cracks leading to fracture. Multi-activation of fractures is caused by impact loading. Because crack growth occurs so rapidly and the cracks are well distributed throughout the specimen cross-section, all particles of the material are accelerated by the pulse, preventing the load from being concentrated only on the weakest point; by applying the loading wave, several weak points are simultaneously fractured. Fig. 15.7b shows that a single crack propagates through the cross section at a strain-rate of 1 s^{-1}, covering the entire cross section in about 50 μs.

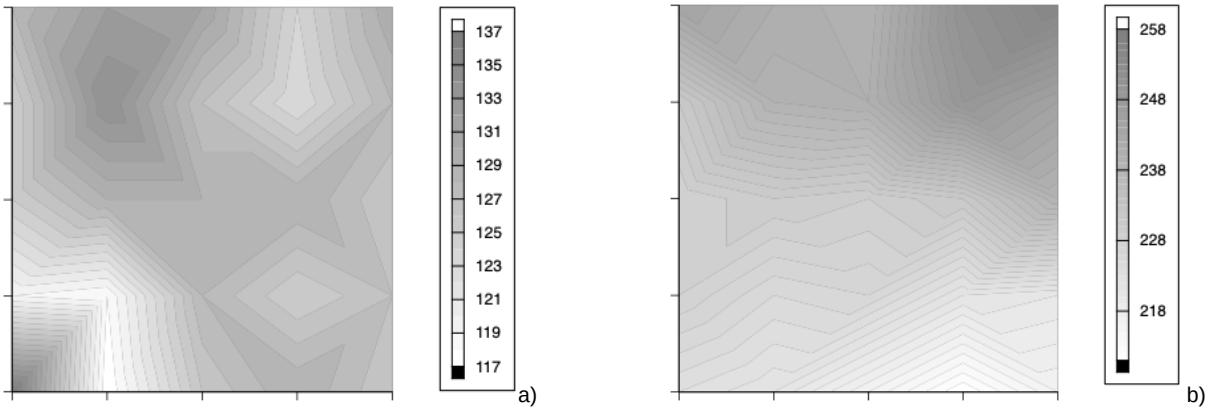

Figure 15.7 – Crack propagation pattern in two concrete specimens at two strain rates: a) @10 s^{-1}; b) @1 s^{-1}.

Using the bundle information, local strength can be determined. A similar value can be observed by comparing the mean values of these local strengths to those obtained with the signal from the non-divided output bar. Strength differences can be attributed to aggregates and their distribution in the cross-section. Comparison of strength distribution with crack propagation pattern in Fig. 15.8 illustrates this fact.

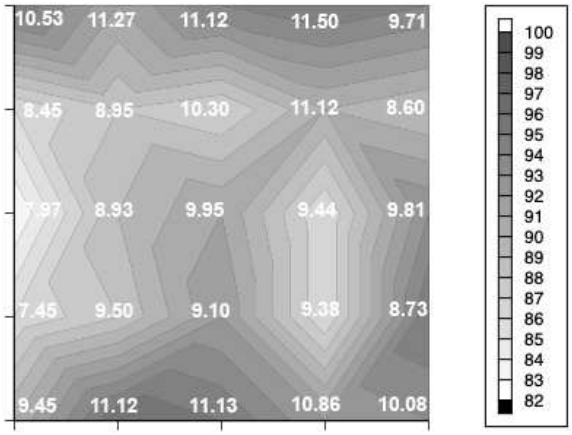

Figure 15.8 – Crack pattern and local strengths distribution over the cross-section of a concrete specimen during a tensile test @10 s^{-1}.

15.4 Experimental methods

Given the sensitivity of concrete to loading rate and loading path a wide variety of experimental methods have been developed for several decades to characterise the dynamic behaviour of concrete. A summary of experimental methods classified by testing apparatus is gathered in Table 15.1. Hydraulic or electromechanical presses have the advantage of making it possible to load samples or substructures according to a wide variety of loading type and loading rate. Deformation controlled tests can be performed making it possible to identify the rate effects on strength and softening behaviour. However, mainly due to limited bandwidth of load sensor they are unsuitable to high-rates requiring short loading times. Split Hopkinson bar apparatus made of input and output bars have been widely used for tensile, compression or shear testing of concrete. However, as usual, loading time is restricted to wave round-trip time in Hopkinson bar, but should also be large enough compared to the wave round-trip time in the tested sample to unsure the desired mechanical

balance of the sample. These two constraints restrict the range of permissible strain-rates, especially in tensile loading. Shorter loading time can be considered in spalling tests performed with a single Hopkinson bar or with plate-impact facility. However, it relies on an indirect measurement of strength and the post-peak behaviour and fracture energy are much harder to characterize. Other dynamic experiments such as the edge-on impact test give the possibility to analyse the fracturing process by means of ultra-high speed imaging or post-mortem observation. However, such experimental techniques do not give access to direct measurement of strength or fracturing energy. These experimental methods are described with more details in the following subsections.

Table 15.1. Main advantages, drawbacks and limitations of testing method and apparatus used to characterize the dynamic response of concrete over a wide range of strain-rate.

Testing apparatus	Loading type	Advantages	Limitations	Range of strain-rates
Hydraulic presses, electromechanical presses, high speed jacks	Tension, compression, triaxial compression, confined shear, mode I/II fracture	High loading capacity Testing of large sample or subscale structure Displacement or load controlled	Limited bandwidth of load sensor Unsuitable for short loading time (< 100 µs)	From quasi-static to a few 1 s^{-1}
Split Hopkinson bar with sample in balance state	Tension, compression, confined compression and shear, mode I/II fracture	Simplicity to use and non-expansive testing	Non-constant strain-rate (proportional to eR) $T_{load} < T_{round\text{-}trip\ in\ HB}$ $T_{load} > T_{round\text{-}trip\ in\ sample}$ Limited range of oading	Tension: from a few $1s^{-1}$ to a few 10 s^{-1} Compression and shear: from a few $1s^{-1}$ to a few 100 s^{-1}
Single Hopkinson bar with sample in unbalance state	Spalling test, rock spall test	Simplicity to use and non-expansive testing High-rate of loading	Short loading time: $T_{load} < T_{round\text{-}trip\ in\ sample}$ Indirect measurement of strength, non-constant strain-rate, Post-peak response difficult to characterize	Tension: a few 10 s^{-1} to a few 100 s^{-1}
Plate-impact or pulsed power technology	Spalling test, 1D-strain compression	High strain-rate and stresses, EOS	Very short loading time: $T_{load} < T_{round\text{-}trip\ in\ flyer}$ $T_{load} < \varnothing/(2.C_{wave})$ Cost of facility No visualization with high speed camera	Shockless plate-impact or pulsed current: a few 10^3 s^{-1} to a few 10^5 s^{-1}
Edge-on impact	Divergent wave, shear fracture from front edge, radial cracking, spall fracture	Simplicity to use and non-expansive testing High-rate of loading Visualisation of fracturing by means of high-speed camera	No measurement of strength. Classical EOI: surface or post-mortem visualisation	A few 10^2 s^{-1} to a few 10^3 s^{-1}

15.4.1 Tensile testing of plain concrete in balance state

During the past few decades, experiments made using Hopkinson or Kolsky bars have become increasingly popular as an effective method of capturing bulk behaviour for cementitious specimens when they are loaded dynamically, as compared to other experimental methods. In the case the sample taped to the input and output bars a mechanical balance of the specimen is pursued. Input and output forces are expected to be close to each other and inertial effects within the sample are supposed negligible in comparison to the level of loading applied to the specimen. Thus, a correct balance of the specimen is assumed in each method. Equality of input and output forces implies a short round-trip time in the specimen in comparison with the loading time to failure as expressed in Equation (15.1):

$$T_{loading} = \frac{\varepsilon_{failure}}{\bar{\dot{\varepsilon}}} >> T_{sample\ round-trip} = \frac{2L_{sample}}{C_{wave}}, \quad (15.1)$$

where L_{sample} and C_{wave} are respectively the sample length and 1D-wave speed of concrete, $\bar{\dot{\varepsilon}}$ is the mean strain-rate and $\varepsilon_{failure}$ is the failure strain. An estimation of the maximum strain-rate providing more than 5 wave round-trips in concrete sample before failure is reported in Table 15.2 considering various levels of failure strain. Given the small failure strain of concrete in tension, strain-rate should not exceed a few 1 s^{-1} to guarantee a correct mechanical balance of concrete sample. To do so, pulse-shaping techniques, such as a small ring of lead at the projectile-input bar interface, can be used to decrease the slope of rising edge of the incident wave, so the loading rate is decreased in the tested sample.

Table 15.2. Estimation of the maximum strain-rate ensuring at least 5 wave round-trip in concrete sample before failure.

L_{sample} (mm)	C_{wave} (mm/µs)	$5 \times T_{wave\ round-trip}$ (µs)	$\varepsilon_{failure}$	Max ($\dot{\bar{\varepsilon}}$) (s^{-1})
40	4	100	1e-4	1
40	4	100	2e-4	2
40	4	100	5e-4	5
40	4	100	1e-3	10
40	4	100	1e-2	100

The Hopkinson Bar Bundle system (HBB) presented in the previous subsection (15.3) allows precise measurement of the stress-strain response, including the softening behaviour of concrete. More traditional Split Hopkinson (Kolsky) Tensile Bar can be considered for dynamic tensile testing of concrete as depicted on Fig. 15.9. A tubular striker hits an anvil fixed to the input bar. The incident tensile wave travels upstream through the input bar. A part of this pulse that represents the strength of the concrete specimen is transmitted to the output bar (transmitted wave) whereas the other part reflects back and travels downstream through the input bar (reflected wave). A classical Kolsky processing of data (from incident, reflected and transmitted waves measured from strain gauges attached to input and output bars) provides the temporal profile of forces, velocities and displacements on each side of the sample from witch the stress-strain response can be deduced.

Figure 15.9 – Traditional Split Hopkinson (Kolsky) Tensile Bar for tensile test.

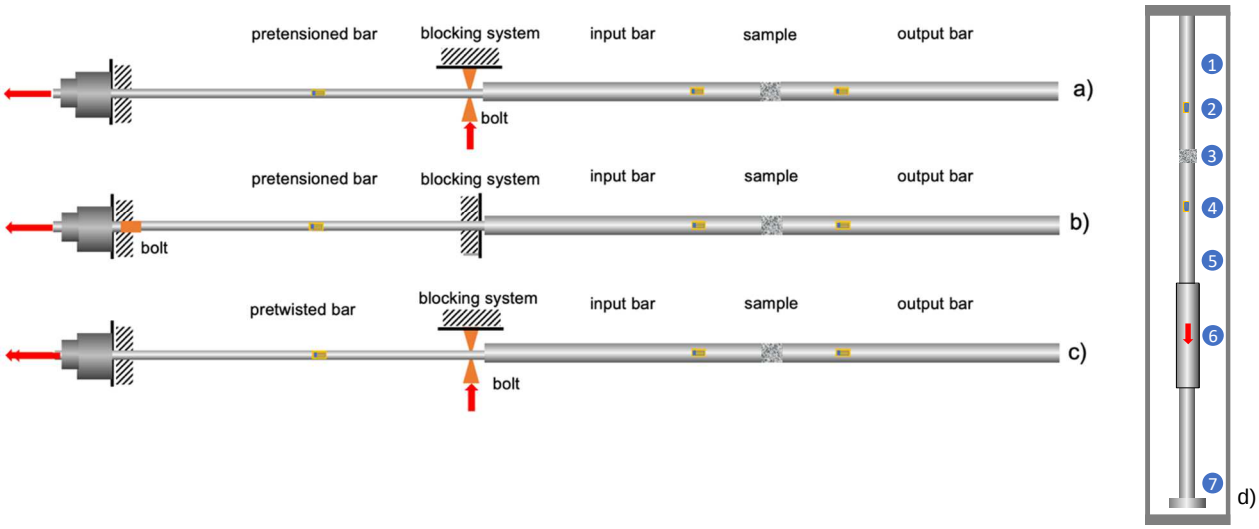

Figure 15.10 – Modified Split Hopkinson Bar with pretensioned bar for: a) tensile test; b) compression test; c) torsion test; developed at JRC and at SUPSI. Traditional Split Hopkinson (Kolsky) bar for tensile test by using falling mass. Gravity driven SHB facility developed at TU-Delft; d) (1. output bar; 2. output strain gauge; 3. concrete sample; 4. input strain gauge; 5. input gauge; 6. drop weight; 7. anvil at bottom end.).

The modification of the Split Hopkinson bar introduced by Albertini and Montagnani in seventies, named Modified Hopkinson Bar technique, was extensively used to characterize concrete and quasi-brittle materials [Cadoni and co-workers]. Fig. 15.10 a-c depict three different set ups dedicated to tensile, compression and torsion tests, respectively. The diameter of the bars and specimens ranged between 20 to 60 mm. The application of the Modified Hopkinson Bar technique allowed for the investigation of concrete's response under high strain rates. By employing this method, significant phenomena that occur during the direct tension loading of plain concrete at high strain rates have been successfully observed. Moreover, this technique exhibits remarkable precision in replicating both the ascending and descending portions of the stress-strain curve of a material.

A derivative of Split Hopkinson (Kolsky) Tensile Bar called the gravity driven SHB facility was developed at TU-Delft in the 1980s by Reinhardt and co-workers (Fig. 15.10 d). This facility, which consists of two cylindrical aluminium bars (Ø 74mm) between which the concrete specimen is bonded, was used by several researchers in the past [Kormeling, Zielinski, Rossi, Toutlemonde, and Weerheijm] to characterize the tensile strength and post-peak response of concrete at different moisture levels and considering different aggregate sizes and water to cement ratio [Toutlemonde, 1994]. The loading rate was derived from the slope of the transmitted stress pulse. The dynamic fracture energy was also investigated by Vegt et al [2007]. To do so, notched specimens were used to avoid multiple fracture and two displacement transducers were attached to the aluminium bars on both sides of the specimen to obtain the stress-deformation curve, and thereby the fracture energy for a single fracture zone.

15.4.2 Tensile testing in unbalance state and 1D-stress condition (single Hopkinson bar)

The spalling technique based on the use of a single Hopkinson bar was pioneered by Klepaczko and Brara [2001] and the processing methodology was successively discussed and improved by Schuler et al [2006], Erzar and Forquin [2010] and Forquin and Lukic [2018]. It allows reaching much higher strain-rates than classical SHTB device. The principle of the spalling test is depicted in Fig. 15.11. A compressive pulse is generated on one end of a metallic (steel or aluminium alloy) Hopkinson bar by using short cylindrical projectile launched by a gas gun facility or by using a small explosive charge. In the case of projectile impact, the pulse length defined by the striker length and wave speed and by the contact conditions at projectile-input bar interface should be short enough compared to the concrete sample length to generate a tensile failure in the concrete sample. Indeed, the compression pulse travels through the Hopkinson bar towards the contact surface of the concrete sample and is partially transmitted to the sample depending of the impedance mismatch between the metal of the bar and the concrete. This transmitted compression pulse reflects as a tensile wave on the sample free-end traveling downstream into the specimen. When the tensile wave exceeds in amplitude the compression pulse a tensile loading spreads out the concrete sample leading to its tensile damage and/or failure depending of the loading amplitude compared to the tensile strength of the sample. Given the small diameter of the sample in comparison to its length and due to wave dispersion phenomena acting in the input bar (filtering the highest frequencies that compose the incident pulse) a quasi-uniaxial (1D) stress state can be assumed in the concrete sample (providing that a plane contact is achieved between the sample and Hopkinson bar contact surfaces):

$$\bar{\bar{\sigma}} = \begin{bmatrix} \sigma(x,t) & 0 & 0 \\ 0 & 0 & 0 \\ 0 & 0 & 0 \end{bmatrix}_{(\bar{e}_x, \bar{e}_y, \bar{e}_z)} , \; \bar{v} = v(x,t)\,\bar{e}_x \,, \; \sigma(x,t) = \pm\rho\, C_{wave}\, v(x,t) \,, \tag{15.2}$$

The main advantages of this technique are the following: on one hand no adhesion or bonding is needed at the sample input bar interface although the setting up of the sample requires special care. Moreover, limitations regarding the level of strain-rate to ensure a balance of the specimen vanish since this hypothesis is unnecessary in the data processing. The main drawbacks and limitations are the following: this technique is restricted to a small range of strain-rates (about 20 s^{-1} to 200 s^{-1}). Indeed the loading-rate is limited by the amplitude of the compression pulse that should not exceed the sample compression strength (given that the compression wave precedes the tensile loading). The applied strain-rate is also conditioned by the shape of the incident wave, which is influenced by the projectile geometry (length, diameter...), the use of pulse-shaping and by the wave dispersion phenomenon that is related to the input bar length and diameter.

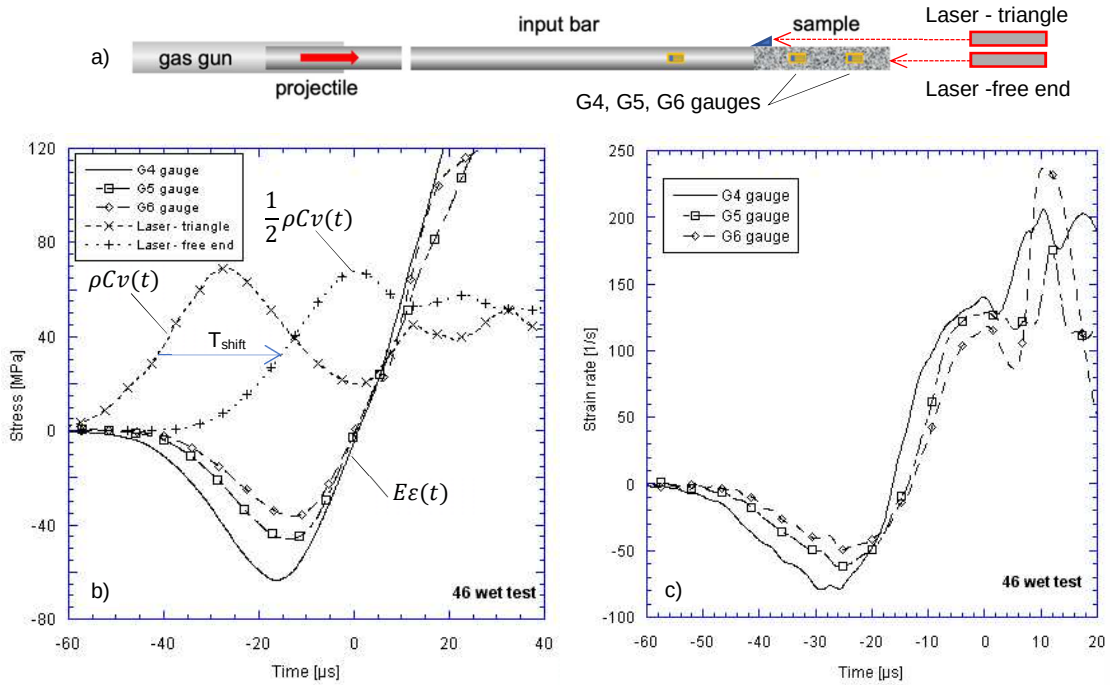

Figure 15.11 – a) Traditional Hopkinson bar for spalling test, b) Data from strain gauges and laser vibrometer converted into stresses.

Several processing methods used to deduce the dynamic tensile strength were discussed by Erzar and Forquin [2010] relying on the results of numerical simulations. It was concluded that Novikov's formula provides a quite good approximation of the tensile strength. First, the 1D-wave speed is deduced by calculating the traveling time of the compression pulse from a point attached to the sample near the contact side to a point located on the sample free-end. To do so, a longitudinal strain-gauge (or a laser vibrometer) can be used near the contact surface and a laser vibrometer pointed out toward the sample rear face can be used to measure the velocity profile on it:

$$E_{dynamic} = \rho\,(C_{wave})^2 \quad with \;\; C_{wave} = \frac{L_{contact \rightarrow free-end}}{T_{shift}} \quad . \tag{15.3}$$

The mean density of tested concrete being known the dynamic Young's modulus can be deduced (Eq. 15.3). Next, the apparent failure strength (also called spall-strength) is calculated according to the Novikov's formula:

$$\sigma_{spall} = \frac{1}{2}\rho\, C_{wave}\, \Delta v_{pb} \quad , \tag{15.4}$$

where Δv_{pb}, called the pull-back velocity, represents the difference between the peak of particle velocity and the velocity at the first rebound both measured on a point of the sample free-end.

The main limitation of this "classical" processing method, based on the "Novikov's acoustic approximation" and the rear face velocity measurement, is that it relies on the assumption according to which the material behaves linear-elastically up-to the peak tensile stress when an "instantaneous failure" occurs which generates the velocity rebound on the rear face. However, tensile failure in concrete is not instantaneous and a non-symmetric response in compression and tension, even prior the stress peak, can be observed, especially in dry concrete. This point was especially addressed in [Forquin and Lukic, 2018] by considering, in a numerical simulation of a spalling test, different values of Young's modulus in compression and tension and by comparing the spall strength from Novikov's equation to the tensile strength imposed to the concrete (Table 15.3). Finally it was concluded that the mismatch made with Novikov's equation increases with a dissymmetry factor deviating from one.

Table 15.3. Numerical simulations of a spalling test considering different dissymmetric parameter ($\alpha = E_t/E_c$) and an imposed tensile strength equal to 7 MPa.

Dissymmetry factor	Pullback velocity	Novikov's formula
$\alpha = E_t/E_c$ [1]	Δv_{pb} [m/s]	σ_{spall} [MPa]
1	1.56	7.04
0.75	1.84	8.31
0.5	2.95	10.0

The so-called Image-Based Inertial Impact (IBII) data processing based on the virtual fields method (VFM) introduced in [Pierron and Forquin, 2012] allows circumventing these difficulties. The VFM is based on the use of the principle of virtual work:

$$\underset{(1)}{-\int_V \sigma : \varepsilon^* dV} + \underset{(2)}{\int_{\partial V} \mathbf{T} : u^* dS} + \underset{(3)}{\int_V \mathbf{f} : u^* dS} = \underset{(4)}{\int_V \rho \mathbf{a} . u^* dV} \quad , \tag{15.5}$$

where σ is the actual stress tensor, ε^* is the virtual strain tensor, **T** is the vector of surface distribution of applied loading acting on the solid boundary ∂V, u^* is the virtual displacement vector, **f** is the vector of distribution of volume forces acting on the solid volume V, ρ is the mass per unit volume, **a** the acceleration vector. '.' stands for the scalar product between two vectors and ':' stands for the contracted product between two second order tensors.

Next, by considering specific virtual displacement fields, the acceleration map ($a_x(x, t)$) can be used as an alternative 'load cell' to identify constitutive material parameters. For instance, if ones assume that the stress state is uniaxial and the material remains in its elastic domain ($\sigma_{xx} = E.\varepsilon_{xx}$), the dynamic Young's modulus (E) can be calculated in the following way. Let's consider a window of length (L-x_0) where $x = L$ corresponds to the sample free-end so $\mathbf{T}(x = L) = 0$. Next, by considering a virtual field satisfying the following condition:

$$u^*(x) = f(x - x_0) \;\text{ with }\; f(0) = 0 \quad , \tag{15.6}$$

the second term of Eq. (15.5) vanishes and the principle of virtual work can be rewritten to get the average Young's modulus at each time step of the test:

$$\bar{E}_{dyn}(t) = \rho \left(\frac{\overline{a_x(t) f(x - x_0)}}{\overline{\varepsilon_x(t) f'(x - x_0)}} \right) \quad , \tag{15.7}$$

where the fields of virtual work $a_x(t)\, f(x\text{-}x_0)$ an $\varepsilon_x(t)\, f'(x\text{-}x_0)$ are averaged from the cross-section (x_0) to the free-end. The best virtual field that maximize both terms of the fraction of Eq. (15.7) are discussed in [Pierron and Forquin, 2012; Forquin and Lukic, 2018]. An example of result obtained according to this processing method in the case of a spalling test performed on dry common concrete at 100 s^{-1} is presented in Fig. 15.12a. The full-field measurement was performed thanks to the grid method (1 mm pitch) with a field of view set to 24 x 60 mm and thanks to UHS (digital Ultra-High-Speed) (HPV1 Shimadzu) camera with an interframe time set to 0.5 or 1 µs. Finally, the time resolved Young's modulus plotted on the Figure 15.12a reveals a dissymmetric elastic modulus between the compression (≈ 33 GPa) and tensile stages (≈ 19 GPa) prior the tensile fracture. Furthermore, it is possible to reconstruct the mean axial stress in any cross-section and at any instant visualized with the UHS camera by introducing a rigid body like virtual field. In such case, the virtual strain tensor ε^* being equal to 0, the first term of Eq. (15.5) vanishes and the principle of virtual work reads:

$$\sigma(x_0, t) = \rho\, (L - x_0) \overline{a_x(t)} \quad , \tag{15.8}$$

where (L-x_0) is the length from the considered cross-section (x_0) to the free-end and ($a_x(t)$) is the mean acceleration averaged from (x_0) to the free-end. An example of processed data considering two cross-sections located at 40 and 50 mm from the free end is illustrated in 15.12c. The compression loading leaves room to a uniform tensile leading at t = 60 µs. The maximum tensile stress (about 7.5 MPa) is observed to be significantly smaller than the spall strength provided by Novikov's formula (about 10.6 MPa), which is a consistent result with the results of numerical simulations (Table 15.3). The full-field measurement also provides the change of strain with time at the same cross-sections so the stress-strain response can be deduced (Figure 15.12d). A linear response is noted in the compression regime. In the tensile regime, a lower slope (about 19 MPa) is noted prior the peak, which is consistent with the previous result (Figure 15.12a). In addition, multiple cracking of the sample after the peak is revealed by several discontinuities in the field of displacement (Fig. 15.12b). The softening behaviour makes it possible to deduce fracture energy of concrete as briefly presented hereafter.

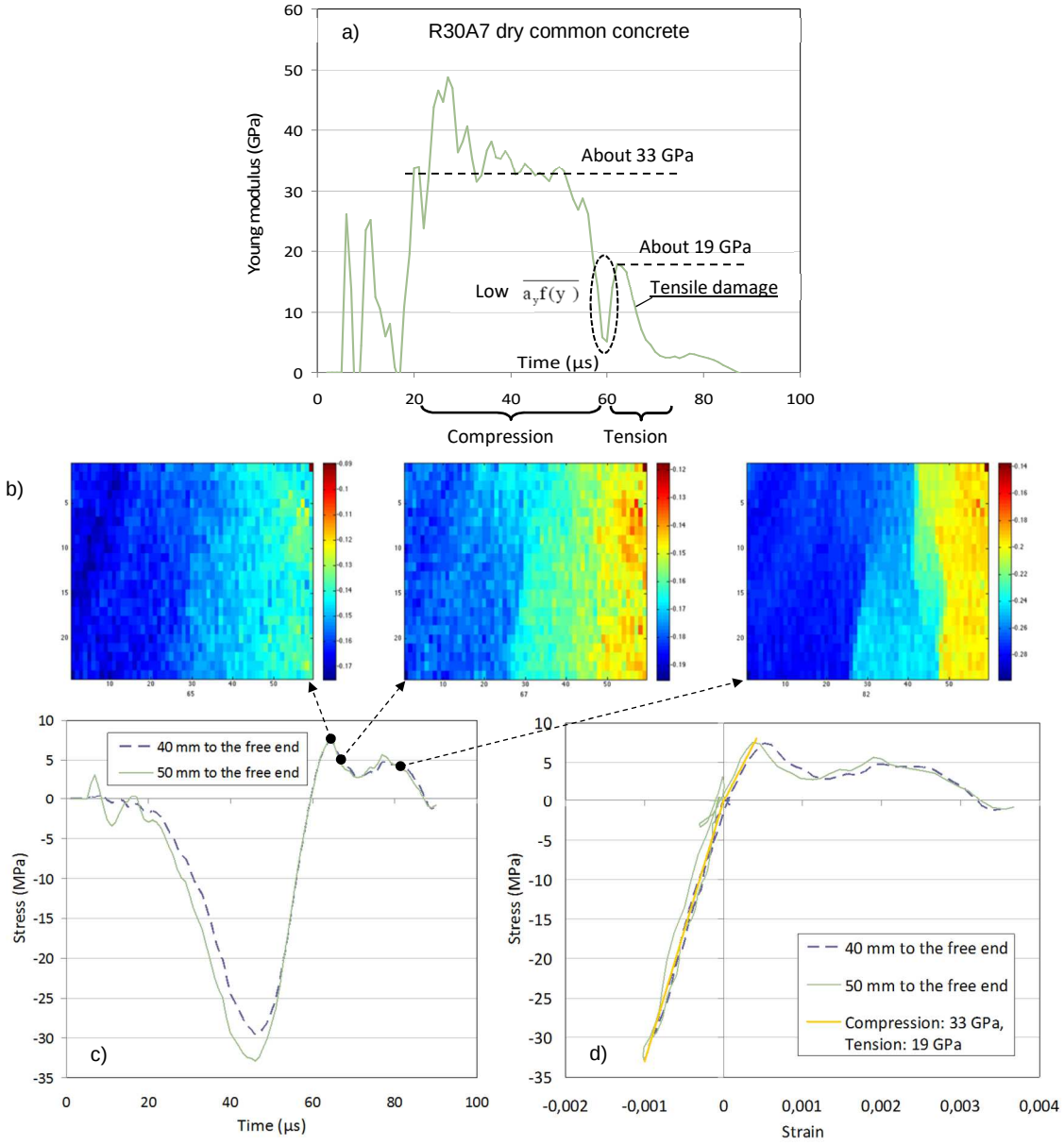

Figure 15.12 – Spalling test performed with dry ordinary concrete and processed with full-field measurement along with the VFM [Forquin and Lukić, 2018] a) Time-resolved Young's modulus, b) discontinuities of the displacement field at different times, c) Time-resolved stress at 40 and 50 mm from the free-end, d) Stress-strain responses in the same cross-sections. For a color picture the reader is referred to the electronic copy of this book

The Image-Based Inertial Impact (IBII) can be also used to deduce the dynamic fracture energy of concrete. Indeed, as illustrated in Figure 15.12c, the IBII data processing of spalling test already gives the temporal evolution of mean axial stress in any cross-section visualised with the ultra-high speed camera (Eq. 15.8) providing the post-peak softening behaviour of concrete. Next, a 'differential displacement gauge' can be introduced to calculate an inelastic differential displacement around the "dominant" macro-crack providing a Crack-Opening-Displacement quantification (Figure 15.13a). Thereby, the stress-COD curve can be plotted for each visualized dynamic fracture (Figure 15.13b), from which the concrete specific fracture energy per macro-crack can be obtained according to:

$$G_f^{COD} = \int_{u(\sigma=\sigma_{max})}^{\infty} \sigma(u_{COD})\, du_{COD} \quad , \tag{15.9}$$

Experimental results of fracture energy versus crack opening rate extracted from [Lukic et al, 2018] are reported in Figure 15.13c along with data from the literature and CEB model predictions. Whereas the experimental values were obtained in the same range of crack-opening-rate the values of specific fracture energy are observed to be lower than the results obtained with other method. At this stage, the data are few and still need to be consolidated but this technique exhibits obvious advantages compared to previous methods. Indeed, it is valid without assumption on the material constitutive behaviour and it does not require performing any notch in the tested sample. A comparison with notched samples constitutes a possible prospect for further works.

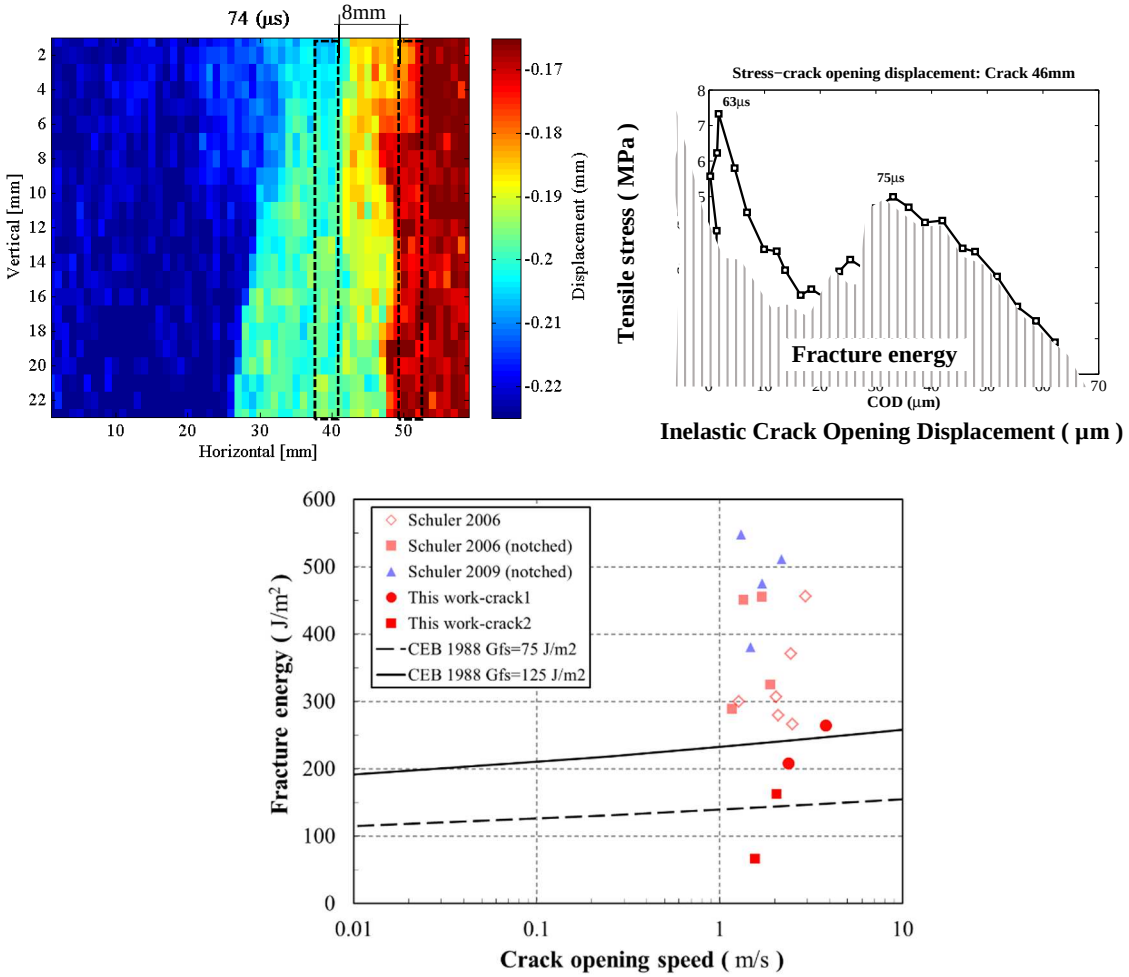

Figure 15.13 – a) Differential displacement gauge considered to deduce the COD quantification around the "dominant" macro-crack, b) Stress-COD curve, c) Fracture energy obtained from the IBII technique compared to data from the literature and CEB model predictions. [Lukic et al, 2018]. For a color picture the reader is referred to the electronic copy of this book.

It should be pointing out is that equations (15.7, 15.8 and 15.9) are independent regardless to the material constitutive behaviour as they are obtained from the principle of virtual work which is a simple reformulation of Newton's second law and conservation of momentum. In addition, the displacement fields from which the acceleration fields are deduced are obtained with non-contact optical measurements. Nevertheless, this processing that relies on a double temporal derivation of displacement fields is strongly related to any source of noise coming from the full-field measurement technique (quality of the grid…) and from the acquisition system (quality of pictures of the ultra-high speed camera, flickering…). For this reason this Image-Based Inertial Impact testing technique should still be considered as a technique under development although it is promising.

15.4.3 Tensile testing in unbalance state and 1D-strain condition (plate impact)

Spall test by plate impact is a convenient technique to characterize the dynamic strength of materials at high rates [Antoun et al., 2002]. In these tests, a thin disc launched at a velocity of few tens to few hundreds of meters per second hits a plate (target) of thickness much smaller than its lateral dimensions. Compressive waves propagate in the flyer plate and in the target, reflect as release waves on free surfaces of the target and projectile. A fast dynamic tensile loading initiates when

both release (decompression) waves cross each-other leading to a dynamic failure in a 1D uniaxial strain-state. The spall strength can be again deduced from the formula proposed by Novikov et al [1966]:

$$\sigma_{spall} = \frac{1}{2}\rho\, C_{Longitudinal}\, \Delta v_{pb} \quad , \tag{15.10}$$

where Δv_{pb} denotes the pull-back velocity corresponding again to the difference of velocities between the maximum value and the velocity at rebound both measured on the rear face of the specimen, ρ is the density and C_L denotes the longitudinal wave speed that is expressed as (in linear isotropic elasticity):

$$C_L = \sqrt{\frac{E(1-\nu)}{\rho(1+\nu)(1-2\nu)}} \quad , \tag{15.11}$$

where E and ν are respectively the Young's modulus and Poisson's ratio. The spall strength of mortar specimens was investigated by Grote et al [2001] by using a PMMA striker (Fig. 6-24). The experimental results Has shown that the higher the impact velocity the lower the spall strength. For instance with the lowest impact velocity (89 m/s) the spall strength was 42.3 MPa whereas it was lowering to 33.9 MPa and 12.7 MPa at higher impact velocities (respectively 290 and 408 m/s). The compressive pulse that precedes the tensile loading has supposedly weakened the tensile strength of the sample. However, in such "classical" planar plate-impact test the level of strain-rate remains difficult to establish. Indeed the compressive pulse transmitted to the target is usually characterized by sharp rising edge leading to non-constant strain-rate at the location of spall fracture. Moreover, it cannot be easily adjusted by changing the striker speed. Indeed, the striker speed is bounded by a lower limit to ensure a spall failure and by an upper limit to avoid any material damage or inelastic deformation in compression before spalling.

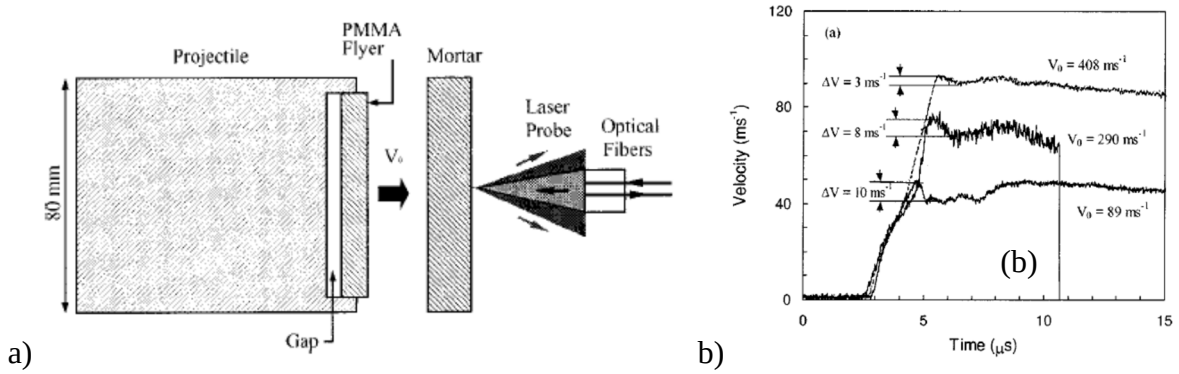

Figure 15.14 – Spalling tests by plate impact technique performed on mortar specimens [Grote et al., 2001] a) Testing configuration, b) Experimental results

A plate-impact technique based on wavy-machined flyer plate was proposed in 2016 to smooth the compression pulse and to better control the applied strain-rate to the target [Forquin, 2016; Forquin and Zinszner, 2017]. In the framework of Brittle's CODEX chair research program conducted in 3SR Laboratory [Forquin et al, 2020], several shockless plate-impact experiment configurations were numerically designed and applied to different kinds of brittle materials (ceramics and ultra-high performance concrete) according to the principle described in Figure 15.15.

Proving that a triangular-shaped compressive wave is generated with the same rising and falling edges, a uniform tensile loading resulting from the superposition of both incident and reflected waves is produced. In addition, considering that both waves propagate at a constant speed (i.e. the longitudinal wave speed) a constant stress-rate is generated prior tensile damage. By changing the loading duration and amplitude of the compression pulse, different levels of stress-rates can be achieved, making it possible to explore the influence of loading-rate on the sample tensile strength of brittle materials.

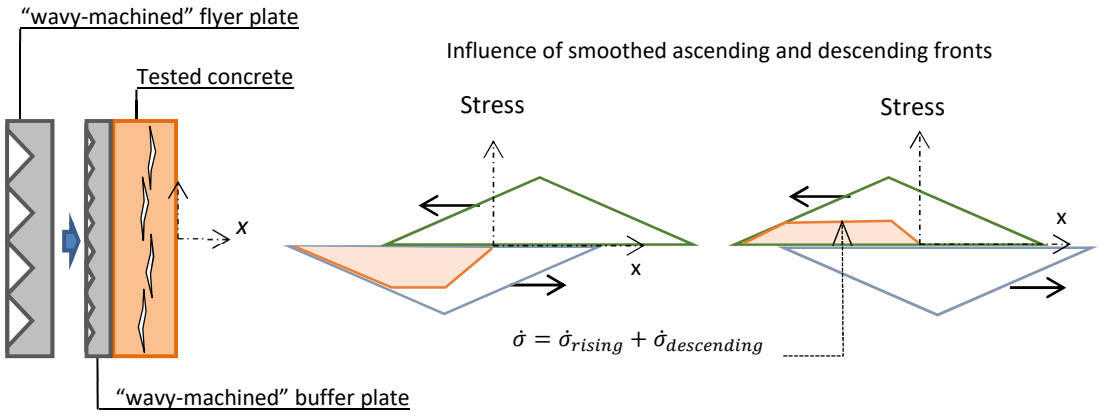

Figure 15.15 – Principle of spalling experiments based on "wavy-machined" flyer and buffer plates. The loading pulse shaped as an isosceles triangle provides a uniform tensile loading with constant stress-rate. (extracted from [Forquin et al, 2020])

A characterization of the tensile strength of a SiC ceramic was proposed in [Dargaud and Forquin, 2021] over a range of strain-rates from 1 600 to 25 000 s^{-1}. The strain rate in the failure zone was evaluated via a numerical simulation, using a damage model and considering the loading deduced from a measurement of particle velocity at the buffer rear free surface. Two experimental configurations were also numerically designed and applied to an UHPC in order to determine its spall strength at strain-rates ranging from 4 000 to 16 000 s^{-1} [Blasone and Forquin, 2020]. The striker made of aluminum alloy and performed with a "toothed" surface on its back is launched against a target that consists in an assembly of a buffer backed with the UHPC sample. The buffer is made of aluminum alloy and is featured with a "twice-wavy-machined" surface on the impact side. This combination allows generating a compressive pulse approaching a triangular shape. By changing the striker velocity and by employing striker and buffer of different dimensions different tensile strain-rates can be reached in the target.

The compression pulse applied to the target can be experimentally characterized thanks to the particle velocity measured on the back surface of the buffer with a laser PDV (Fig. 15.16). A shorter loading time, about 2 µs, is obtained in configuration 2 in comparison with configuration 1. In addition, the amplitude of compression pulse is twice higher. Based on elastic calculations the level of strain-rate in the spalled area is deduced for each configuration (7 270-7 660 s^{-1} in configuration 1 with V_{impact} = 48 m/s and 14 800-15 600 s^{-1} in configuration 2 with V_{impact} = 79 m/s). In addition, the velocity profile measured at the back of the UHPC sample provides the spall strength of the concrete according to Eq. 15.10. Finally, a higher tensile strength (70.1 MPa) was obtained in configuration 1 compared to configuration 2 (84.3 MPa), revealing the strain-rate sensitivity of the tensile strength of the tested UHPC. In conclusion, the shockless spalling configuration based on the use of "back-toothed" striker and "twice-wavy-machined" buffer front surface appears as a promising technique to explore the strain-sensitivity of the tensile strength of concretes a high loading-rates.

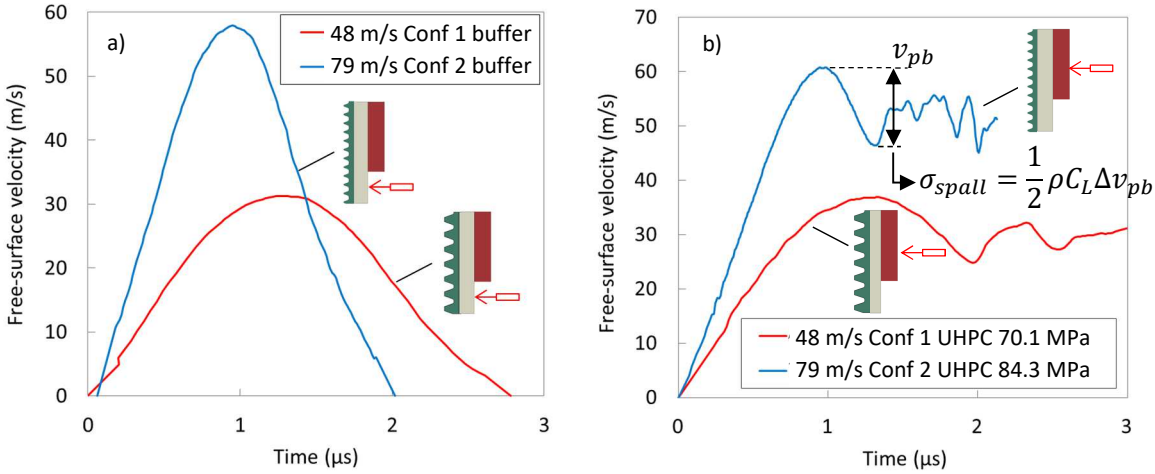

Figure 15.16 – Shock-less spalling experiments performed on UHPC with "wavy-machined" flyer and buffer plates. a) Loading pulse characterized from the measurement of particle velocity measured at the buffer rear free surface. b) Velocity profile measured at the back of the sample providing the spall strength

15.4.4 Compression testing in 1D-strain (quasi-oedometric) condition

The quasi-oedometric compression testing technique constitutes one of the most convenient and efficient testing methods to characterize the quasi-static and dynamic behaviour of concrete and other rock-like materials under several hundreds to a thousand of MPa of confinement [Burlion et al, 2001; Forquin et al, 2007; 2008; 2010]. A cylindrical sample, confined in a confinement cell that is usually made of steel, is axially compressed by means of two compression plugs of diameter close to the tested sample. An interface product is used to fill the gap between the sample and the inner surface of the cell. Once the sample is inserted in the confinement cell and the compression plugs are put in contact with the top and bottom surfaces of the sample an axial compression is applied. The specimen tends to expand under the effect of its radial expansion and exerts a lateral pressure against the confinement cell. In the course of the test, a rise of both axial and radial stresses is observed in the specimen, which gives a possible reading of the mean stress difference as function of the level of applied pressure (the so-called deviatoric behaviour) and of the diminution of the sample volume with the level of hydrostatic pressure (the so-called hydrostatic behaviour giving access to the concrete compaction law). A strong limitation must be highlighted at that point: since the test is driven only by the axial strain, it provides a single loading path (i.e. the "quasi-oedometric loading path") corresponding to an almost "1D" uniaxial-strain loading path. For instance, it cannot be deduced whether the change of strength is mainly related to the change of axial strain independently of the pressure level or to the increase of hydrostatic pressure independently to the level of axial strain. This drawback could be partially circumvented by considering confining cells providing different radial stiffnesses (i.e. more or less radial deformation for a giving internal pressure). However, this solution is difficult to implement in the case of a cell supporting high internal pressures while remaining in a range of elastic deformation.

The introduction of the sample into the confining ring constitutes a very delicate stage as described in [Forquin et al, 2010]. Indeed, it is of great importance to ensure that the entire gap between the sample and the inner surface of the ring is filled with a polymeric resin that is able to sustain the interfacial pressure between the sample and the confining cell. To do so, the following mounting procedure was proposed: the inner volume of the ring was filled by the bi-components epoxy resin named "Chrysor® C6120" which hardens in less than 24 hours. Next, the concrete specimen scotch taped to the upper plug was introduced so the resin was slowly extruded out and the internal gap between the specimen and the ring was totally fulfilled with the epoxy resin. A special alignment device was developed to align the ring, the sample and the two plugs and to get a uniform thickness of polymeric interface between the confining cell and the cylindrical sample.

The sample diameter is usually more than 4 to 5 times larger than the maximum aggregate size. The length to diameter ratio of concrete sample is between one and two. In addition, the length of the confining cell slightly exceeds the sample length in order to keep the sample inside the cell in particular when a dynamic loading is applied (SHPB device). The outer diameter of the cell is chosen as a compromise between a sufficient strength and stiffness of the cell (large enough diameter) and a good sensibility of strain measurements on the external surface of the cell (small enough diameter). For this purpose the outer diameter to inner diameter ratio varies from 1.4 [Forquin et al, 2008] to 2.8 [Burlion et al, 2001] with a predominance of value around 2.

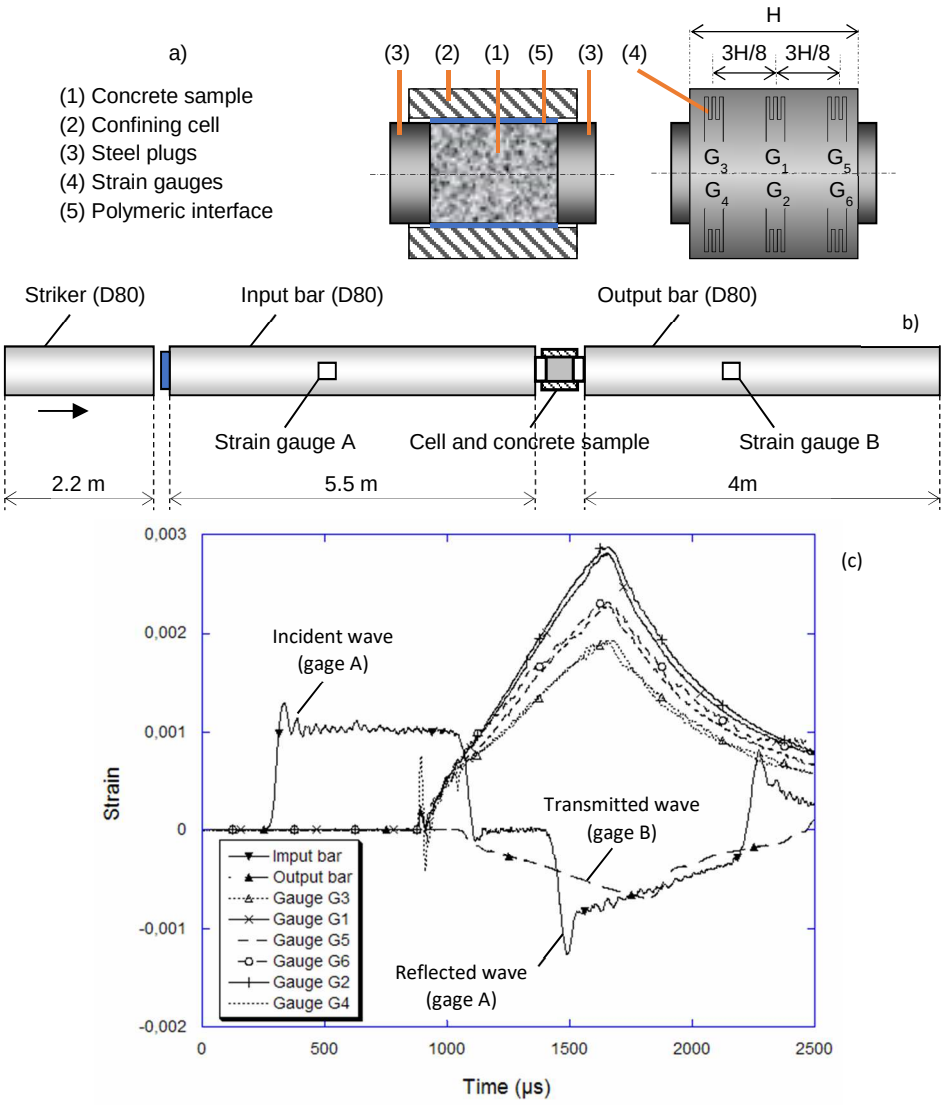

Figure 15.17 – Experimental set-up used dynamic QOC tests. a) Concrete sample in its confining cell, b) Sketch of SHPB system, c) Example of experimental data obtained in [Forquin et al, 2010].

Large diameter SHPB facility is needed to perform dynamic QOC tests applied to concrete. Indeed, reaching an axial stress of 1 GPa in a sample 40 mm in diameter requires a loading capacity of 1250 kN. In [Forquin et al, 2010] the following SHPB set-up was used (Figure 15.17): the striker, the input bar and the output bar are 80 mm in diameter and 2.2 m, 6 m and 4 m long, respectively, and the elastic limit of these elements, made of high-strength steel, is 1200 MPa. When the striker hits the free end of the input bar, a compressive incident wave is generated in the input bar. Once the incident wave (ε_I) reaches the specimen, a transmitted pulse (ε_I) develops in the output bar and a reflected pulse (ε_R) travels downstream in the input bar. The input and output forces and the input and output velocities at the specimen faces are deduced from Kolsky's post-treatment of these waves (cf. Figure 15.17c), thanks to strain gauges glued on the input and the output bars

according to the following equations (without taking into account the wave dispersion phenomena that cannot be neglected with large-diameter Hopkinson bars) [Kolsky, 1949]:

$$\begin{cases} F_{in}(t) = A_b E_b(\varepsilon_i(t) + \varepsilon_r(t)) \\ F_{out}(t) = A_b E_b\big(\varepsilon_t(t)\big) \end{cases}, \tag{15.12}$$

$$\begin{cases} V_{in}(t) = -c_b(\varepsilon_i(t) - \varepsilon_r(t)) \\ V_{out}(t) = -c_b\big(\varepsilon_t(t)\big) \end{cases}, \tag{15.13}$$

where A_b is the area of the input and output bars, E_b corresponds to their Young's modulus and c_b is the speed of a 1D wave propagating in these bars ($c_b = \sqrt{E_b/\rho_b}$), considering ρ_b as the density of the bars. Finally, the mean axial stress and nominal axial strain in the sample are deduced:

$$\overline{\sigma_{axial}}(t) = \frac{F_{in}(t)+F_{out}(t)}{2A_S}, \tag{15.14}$$

$$\overline{\varepsilon_{axial}}(t) = \int_0^t \frac{V_{out}(u)-V_{in}(u)}{h_S} du, \tag{15.15}$$

where h_S is the sample initial length. In addition, the elastic limit of the plugs must be significantly higher than the maximum axial stress reached during the dynamic tests so the elastic shortening of the plugs can easily be subtracted from the total shortening measured.

A processing method was proposed in [Forquin et al, 2007] to deduce the radial stress in the sample taking into account of the barreling deformation of the confining cell and the shortening of the concrete sample during the test but also of the plastic deformation of the steel of which the cell is made. Indeed, it should be noted that, due to the barreling deformation of the cell, the closed-form solution of an elastic ring subjected to a uniform internal pressure along its whole length would provide an erroneous estimation of the radial stress in the tested sample. Therefore, the following methodology can be considered. The constitutive behavior of the constitutive material of the confining cell being known, two calculations are conducted with a FE code considering an internal pressure, which continuously increases up to certain level of pressure (up to 1 GPa for instance), applied to the inner surface of the ring along two different heights h_0 and h_1, these heights corresponding to the initial and final lengths of the concrete sample.
From these calculations the relations: $\sigma_{radial(h_0)} = f_{h_0}\left(\varepsilon_{\theta\theta}^{(G_1,ext)}(t)\right)$ and $\sigma_{radial(h_1)} = f_{h_1}\left(\varepsilon_{\theta\theta}^{(G_1,ext)}(t)\right)$ are deduced, so the radial stress in the sample can be computed knowing the current height of the sample (h_S) according to the following linear interpolation:

$$\bar{\sigma}_{radial}(t) = \left(\frac{h_S(t)-h_1}{h_0-h_1}\right) f_{h_0}\left(\varepsilon_{\theta\theta}^{(G_1,ext)}(t)\right) + \left(\frac{h_S(t)-h_0}{h_1-h_0}\right) f_{h_1}\left(\varepsilon_{\theta\theta}^{(G_1,ext)}(t)\right), \tag{15.16}$$

where $\varepsilon_{\theta\theta}^{(G_1,ext)}$ corresponds to the strain measurement from the strain gauge G_1 located in the symmetry plane of the cell. In a similar way, the (small) radial strain in the sample can be deduced based on the data of hoop strains placed at two locations on the cell ($\varepsilon_{\theta\theta}^{(G_1,ext)}, \varepsilon_{\theta\theta}^{(G_2,ext)}$).

Finally, the deviatoric stress, the hydrostatic pressure and the volumetric strain are deduced:

$$\sigma_{deviatoric} = |\sigma_{axial} - \sigma_{radial}|, \tag{15.17}$$

$$P_{hydrostatic} = -\frac{\sigma_{axial}+2\sigma_{radial}}{3}, \tag{15.18}$$

$$\bar{\varepsilon}_{volumetric}(t) = (1+\bar{\varepsilon}_{axial})(1+\bar{\varepsilon}_{radial})^2 - 1. \tag{15.19}$$

The accuracy and sensitivity of this processing method was discussed in [Forquin et al, 2007; 2008] by processing the data of a series of numerical simulations of QOC test and by comparing the obtained hydrostatic and deviatoric responses to the expected ones (considered constitutive laws for concrete).

Experimental data of dynamic QOC tests performed on dry and water-saturated microconcretes in [Forquin et al, 2010] are reported in Figure 15.18. The experiments performed with samples 30 mm in diameter and 40 mm in length made it possible to achieve hydrostatic pressure up to 1 GPa (Figure 15.18a) and volumetric strain about -10% (Figure 15.18b). The dynamic tests exhibited an important dissimilarity between dry and saturated specimens concerning both deviatoric and hydrostatic behaviors. First, dried microconcretes exhibited a continuous compaction whereas saturated specimens showed a non-linear (hardening) hydrostatic behavior (Figure 15.18c). Moreover, a strong and continuous increase of the strength with pressure was noted with dry samples whereas water-saturated specimens exhibited an almost-perfect saturation of the strength (Figure 15.18d). Quasi-static results allowed highlighting the reason of this dissimilarity. On the one hand, dried specimens behave similarly than dynamic tests and no strain rate effect is observed. On the other hand

the behavior of saturated specimens gradually tends to that of dried specimens when the loading rate is decreased, and an expulsion of water during slow quasi-static tests was observed. Finally, it was concluded that, water-pressure inside saturated microconcrete plays a major role on their fast-quasi-static or dynamic confined behavior by reducing drastically their shear strength. Additional results providing a comparison between static and dynamic responses of common and high-strength concretes are reported in subsection 15.5.

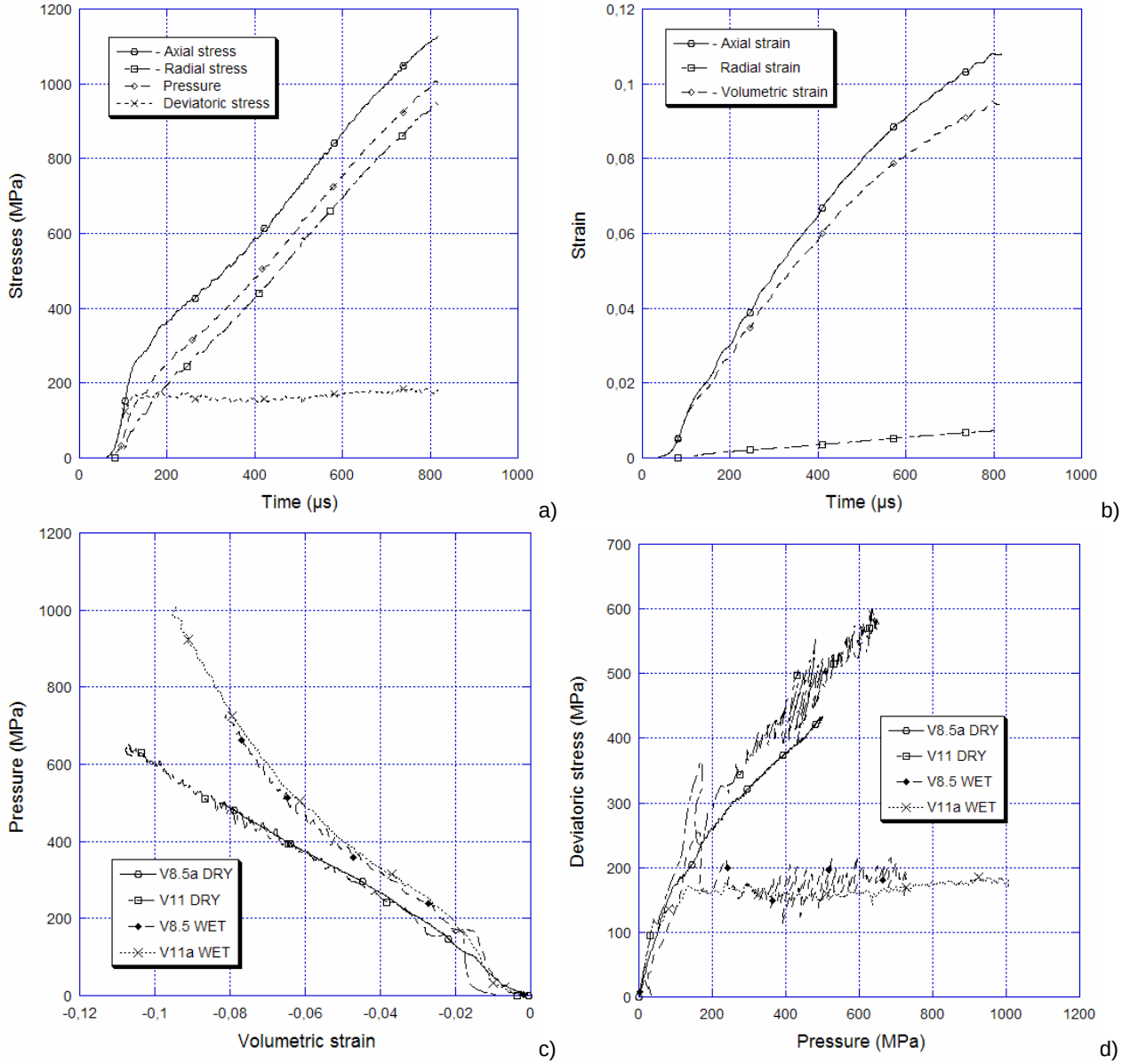

Figure 15.18 – Processed data of QOC tests performed on microconcrete [Forquin et al, 2010]. a) Evolution of stresses, b) evolution of strains in a saturated specimen (V11a-wet). c) and d) Comparison of hydrostatic and deviatoric responses of dried and wet specimens.

15.4.5 Shear testing

The Punch-Through-Shear (PTS) is an experimental technique that allows characterising the confined shear strength and mode II fracture energy of concrete and rock-like materials [Watkins, 1983; Luong, 1990]. Different experimental configurations relying on different types of sample geometries and different ways of applied a confinement to the concrete sample have been developed. In triaxial and Oedo-PTS tests a cylindrical sample is used in which two circular notches are machined on the top and bottom faces of a concrete sample. In triaxial-PTS the specimen is first subjected to a pure hydrostatic pressure whereas an axial load is added in a second step to create a shear fracturing of the ligament [Backers et al, 2002]. However, due to high level of hydraulic pressure to be applied to the sample (a few tens or hundreds of MPa) this technique remains difficult to perform in dynamic conditions. In addition, a self-confinement of the outer part of the sample occurs making it difficult to evaluate the radial stress exerted in the ligament before and during shearing [Abdul-Rahman and Forquin, 2023].

In Oedometric-PTS (Oedo-PTS) experiments, in a similar way than in quasi-oedometric compression tests, a passive confining cell is used instead of hydraulic pressure to apply a confinement to the PTS specimen (Figure 15.19a) [Forquin,

2011]. The length and diameter of the ligament (respectively 10 and 50 mm) provide a shear surface ($S_{lig} = \pi.D_{lig}.H_{lig}$) that should be large enough compared to the cross-section of the largest aggregates of concrete. The inconvenience of Triaxial-PTS (self-confinement) is circumvented by performing several (4 to 6) radial notches in the outer-part of the sample. In addition this testing technique can be easily performed in dynamic conditions by considering an input bar and a tube as output bar (Figure 15.19c). The radial stress in the ligament is deduced from the contact pressure between the sample and the confining cell obtained thanks to the data of strain-gauges attached to the outer surface of the ring.

$$\sigma_{radial} = \frac{S_{contact}}{S_{lig}} P_{contact} \quad with \ S_{contact} = \pi D_{sample} H_{cell}, \tag{15.18}$$

A classical Kolsky data processing can be applied to the recorded incident, reflected and transmitted pulses on the input and output bars so the differential axial displacement of the sample and the input and output forces are deduced. Finally, the mean shear stress in the ligament is deduced:

$$\sigma_{shear} = \frac{F_{axial}}{S_{lig}}, \tag{15.19}$$

An example of result of dynamic Oedo-PTS test performed at a strain-rate about 80 s^{-1} on dry ordinary concrete is given in Figure 15.19e. The shear stress increases until the peak and rapidly decreases after the peak. The maximum shear stress (45 MPa) is significantly higher compared to the value of static shear strength (33 MPa) revealing a significant increase of shear strength (about 36%) from quasi-static to dynamic loading regimes. However, although Oedo-PTS is a convenient technique that can be easily performed in dynamic conditions, it suffers from one important drawback. Indeed confinement level is not constant and is difficult to adjust as it depends on the dilatant behaviour of concrete itself (increase of volume under shearing). It is the reason why another technique was developed called the PS-PTS (Pre-Stressed technique).

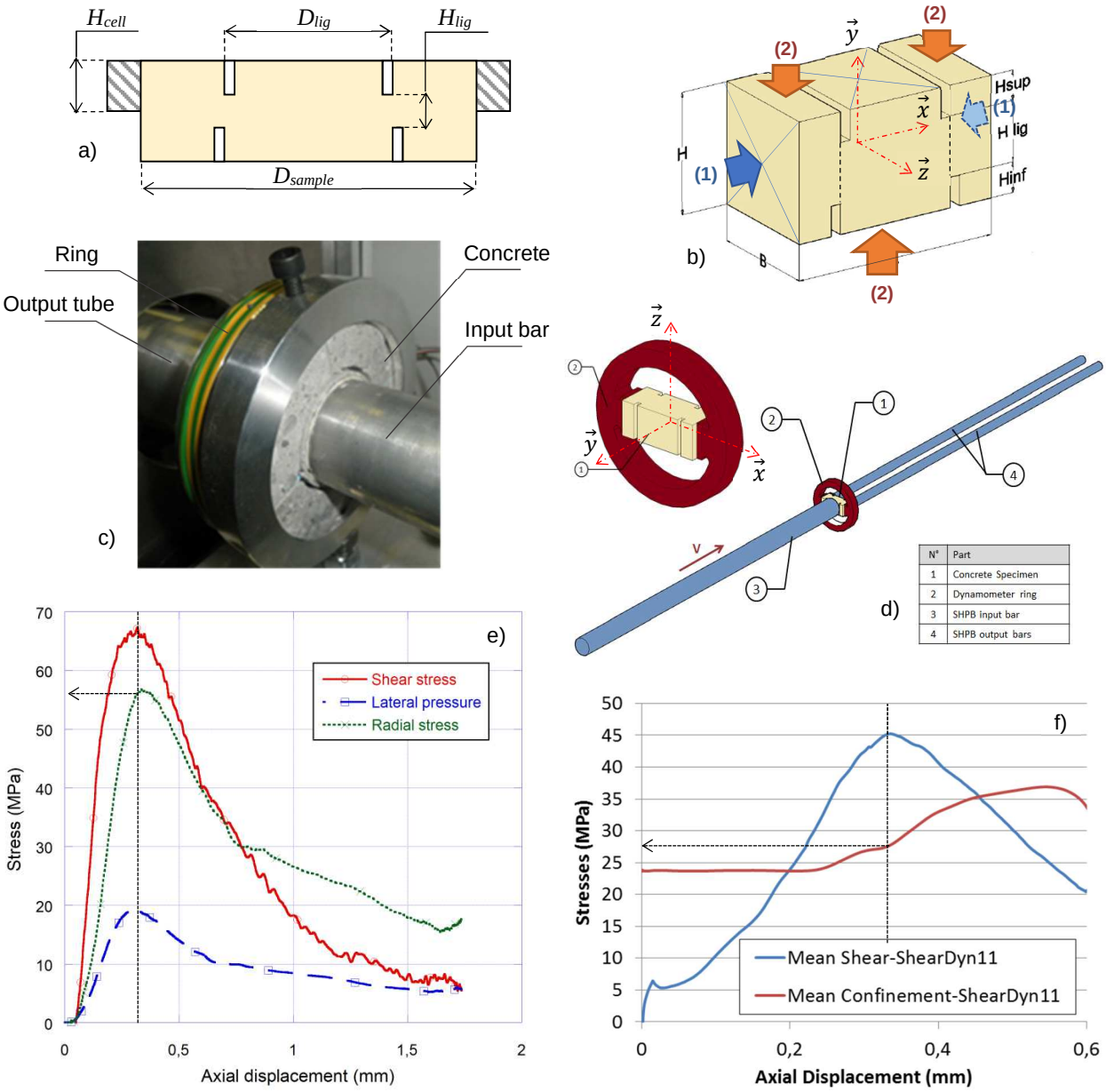

Figure 15.19 – Punch-Through-Shear (PTS) experiments performed in dynamic conditions. a) Oedo (oedometric)-PTS sample geometry, b) PS (Pre-Stressed)-PTS sample geometry, c) Oedo-PTS testing set-up, d) PS-PTS testing set-up, e) Example of oedo-PTS experimental result [Forquin, 2011], f) Example of PS-PTS experimental result [Abdul-Rahman et al, 2021].

The PS-PTS (Pre-Stressed Punch-Through-Shear) technique that consists in shearing a pre-stressed concrete sample benefits from advantages of both (Triaxial and Oedometric) previous testing methods. Indeed, it can be easily performed in static and dynamic conditions, samples are easy to build, it prevents self-confinement issues as in Oedo-PTS but it provides almost constant confinement level at least until the shear stress peak. The geometry of PS-PTS sample proposed in [Forquin et al, 2021], depicted in Fig. 15.19b, corresponds to a rectangular prism in which 4 straight notches are performed. The outer surface of the top notches corresponds to the inner surface of the bottom notches so the fracturing planes are parallel to the (vertical) loading direction. The shear zones correspond to straight planes of height H_{lig} and of width B so the area of the sheared surfaces is $(2.H_{lig}.B)$. The principle of PS-PTS test and data processing was described in details in [Forquin et al, 2021]. First the instrumented cell is deformed elastically by applying a compression load along the axis ($\underline{z}$) until reaching the maximum load ($F_z^{(1)}$) (stage1). When the cell is enough deformed, the concrete sample is inserted into the cell. To increase or adjust the level of pre-stress in the concrete sample, thin metallic sheets are placed in-between the cell and the sample. Next, the compression load (F_z) applied to the cell is progressively released until the sample and the cell are put in contact (stage 2). Finally, (stage 3), the vertical force (F_z) is totally released so the concrete sample is subjected to its final pre-stress confinement level along the direction ($\underline{x}$). In the last stage (static or dynamic test), the central part of the concrete sample is subjected to a relative displacement along the axis ($\underline{y}$) so the two ligaments are sheared (Fig. 15.19d). Finally, although the sheared zone is practically subjected to a constant normal stiffness imposed by the confinement cell, the mean normal stress is close to being constant during the shear loading. This normal stress is directly deduced from the data of strain-gauges attached to the inner or outer surfaces of the metallic cell.

An experimental results obtained in a dynamic PS-PTS test is depicted on the Fig. 15.19f [Abdul-Rahman et al, 2021]. The test was conducted with an initial confinement (normal stress in the ligament) set to 24 MPa. It slightly increases until reaching 27.5 MPa at the peak of shear stress equal to 45 MPa. Finally, the change of confinement stress during the sample shearing, or at least until the peak of shear stress, is much smaller than in the Oedo-PTS test (Fig. 15.19e). Influence of strain-rate and water content on the confined shear strength of concrete is discussed in the next subsection 15.5.

15.5 Plain concrete

In this subsection a set of collected data obtained in static and dynamic experiments was extracted from the literature to illustrate the influence of free water and strain-rate considering 3 types of loading condition: tensile loading, confined shear loading and quasi-oedometric compression. Uniaxial compression was not considered in the present section as the measured axial force (and deduced axial stress) can be influenced by structural inertia at strain-rates above a few tens of s^{-1}. This issue is meant to be avoided in confined shear and quasi-oedometric compression tests as the confinement is supposed to lead to much higher failure strain and loading time.

15.5.1 Influence of strain-rate, free-water and aggregate size on the tensile strength of ordinary concrete

Some experimental results of quasi-static and dynamic tensile tests performed on an ordinary concrete (R30A7) and a microconcrete (MB50) by Erzar and Forquin [2014] are reported in Figure 15.21. “Dry” is defined as “no free water” and “wet” as fully saturated. A little increase of strength is noted from the quasi-static regime to the intermediate strain-rate regime (1e-5 to 1 s^{-1}). This increase of strength is more pronounced with wet concrete than with dry concrete. According to Rossi et al [1992] and Toutlemonde [1994], the rate effect on strength in the moderate regime is caused by the moisture in pores, voids and cracks. The commonly accepted explanation is the so-called Stefan effect [Cotterll, 1964] that describes the pulling force needed to separate two parallel plates at a differential velocity V between which there is an incompressible fluid with viscosity μ. A power law function was proposed by Erzar and Forquin [2014] to describe this effect at the macroscopic scale. According to experimental data obtained with a common concrete, the exponent would be n_{QS} = 0.05 (wet concrete) and n_{QS} = 0.025 (dry concrete).

Spall experiments performed with single Hopkinson bar and processed with Novikov’s formula reveals a strong increase of strength with both dry and wet concretes above a few 10 s^{-1}. In the experimental data reported in Figure 15.21 the dynamic strength of dry concretes (R30A7 and MB50) varies from 8 to 12 MPa whereas the dynamic strength of wet specimens (R30A7 and MB50) varies from 10 to 16 MPa in the explored range of strain-rates (30-150 s^{-1}). Again a noticeable influence of free-water is observed. Finally, both tested concretes (R30A7 and MB50) show similar levels of tensile strength in both dry and saturated conditions, which indicates that the size of the aggregates has a modest influence in this range of strain-rates.

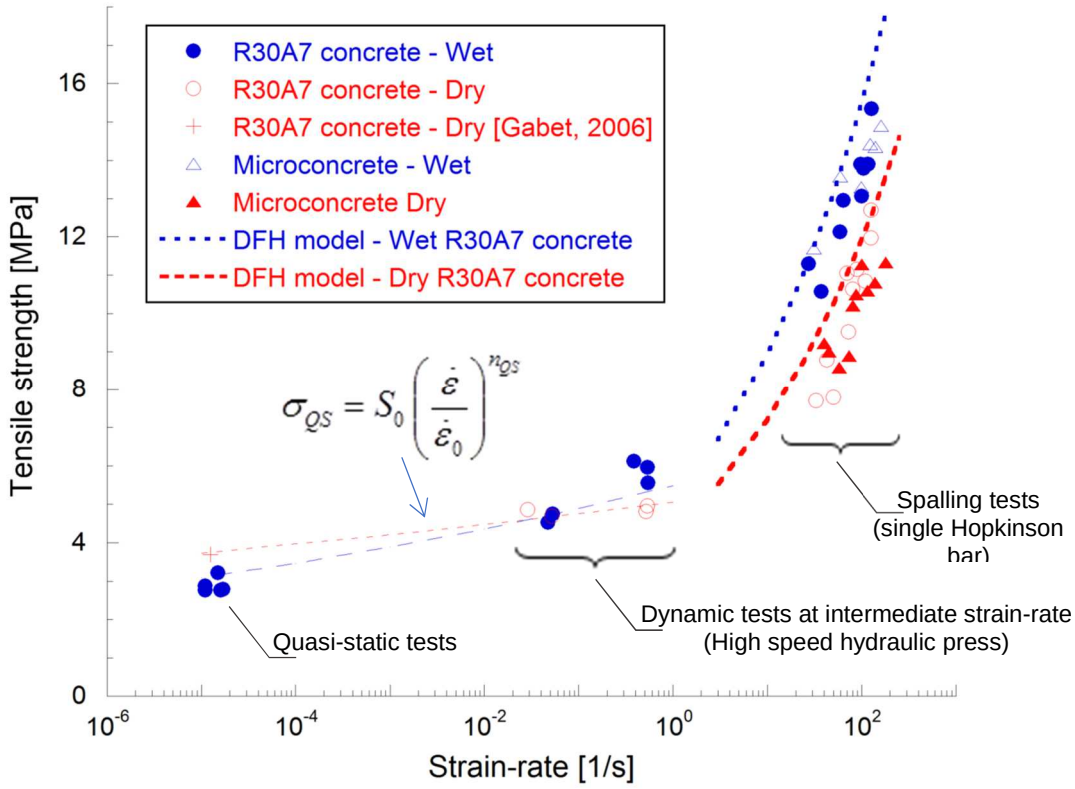

Fig. 15.21. Results of quasi-static and dynamic tests performed with MB50 and R30A7 concretes [Erzar and Forquin, 2011].

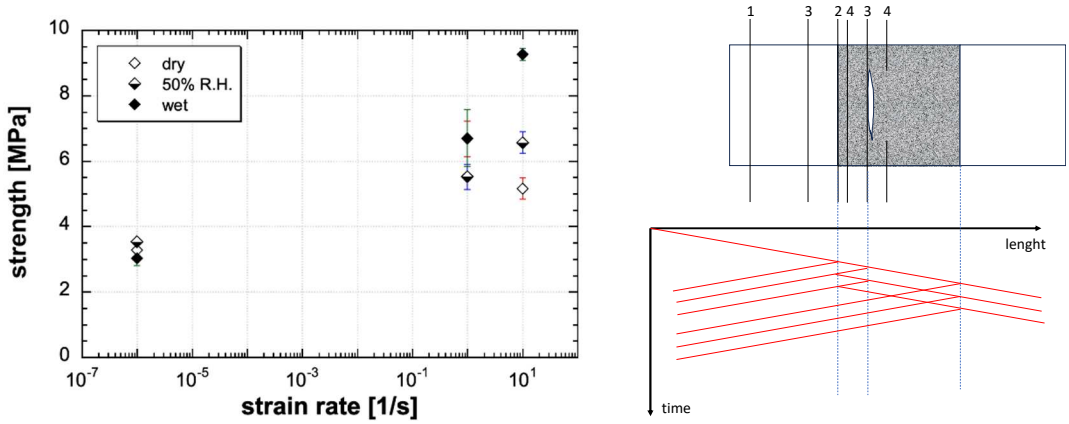

Fig. 15.22. Results of quasi-static and dynamic tests performed with concrete having 10mm aggregate size under dry, 50%R.H. and wet condition [Cadoni et al. 2001].

The increase of the tensile strength with increasing relative humidity [Cadoni et al. 2001] inside the concrete is clearly observed for impact loads such as for for strain-rates above 1 s^{-1} (Fig. 15.22a). A slight decrease of tensile strength is instead noticed for saturated concrete specimens under quasi-static loads. Furthermore, these results show that different levels of free water inside the specimen have an important influence on the sensitivity of the concrete response to the strain-rate. Water-saturated concrete exhibits a significant strain rate dependency. Within concrete, voids are present for various reasons such as the cement hydration process and confined air. The presence of free water within these voids can greatly increase the bearing capacity.The presence of a void leads to a complete reflection of the stress wave at the local level. Since air can be considered as having zero density, the transmitted stress approaches zero. Fig. 15.22b provides a schematic representation of stress wave propagation in the presence of a defect within the concrete specimen. The Figure shows the defect and the wave front at different stages, as well as a Lagrangian diagram. When the stress wave encounters a filled void, the transmitted stress is not zero but rather a non-negligible quantity. Additionally, the reflected stress is not significant enough to cause a local increase in stress that would lead to material damage. Based on this hypothesis, damage in the dried specimen should occur earlier compared to the intermediate and wet conditions as demonstrated in Cadoni et al. 2001. Assuming the end of the linear increase in stress versus time as an indicator of damage, it is evident that damage is more pronounced in the dried specimen as illustrated in chapter 4 dedicated to damage modes in brittle materials at high loading rates. In dynamic direct tensile test the stress-time curve of the dried specimen changes slope at approximately 70% of the maximum stress, while in the specimen cured at 50% relative humidity (R.H.), the slope changes at 83%, and in the saturated specimen, it changes at 94%. Furthermore, the maximum stresses and the times at which

they are reached differ among the dry and wet specimens. This difference can be primarily attributed to the water's effect in the saturated material, as described earlier. Additionally, the presence of micro-cracks in the dried material, resulting from its exposure to the oven, could influence the disparity. In these specimens, the presence of numerous propagating micro-cracks leads to an increase in material damage until macro-cracks form, subsequently decreasing the material's resistance capacity compared to the saturated material.

15.5.2 Influence of strain-rate and free-water on the confined behaviour of ordinary and high-strength concretes

The experimental results of quasi-static and dynamic QOC tests performed on Ordinary Concrete (OC: R30A7 concrete) and High-Strength Concrete (HSC) in dry and saturated conditions are compared in Figure 15.23 [Piotrowska and Forquin, 2015]. On the one hand, in dry condition, both OC and HSC concretes exhibit similar strength with a slightly higher strength of HSC at low pressure but with a more reduced increase of strength with pressure compared to OC (Figs. 15.23 a and b). In addition, it can be noted that the dynamic strength of dry OC and HSC is significantly higher than their quasi-static strength whatever the considered level of pressure. Finally the influence of strain-rate on the confined strength of dry concretes cannot be neglected.

On the other hand, when concrete samples are fully wet, both concretes exhibit completely different strength. In quasi-static conditions a saturation of strength around 70 MPa is observed with OC whereas the strength of HSC goes up to 270 MPa. In dynamic loading conditions, higher strengths are observed with both concretes compared to their quasi-static conterpart showing that the influence of strain-rate cannot be neglected (Figs. 15.23c and d). As in quasi-static loading, the dynamic confined strength of saturated HSC is much higher than in saturated OC. By comparing the confined response of dry and saturated concretes it can be concluded that the confined strength of dry samples is higher than that of saturated samples for both types of concrete. As concluded with microconcrete, it is supposed that water-pressure inside saturated concretes reduces their confined strength. In addition this effect is even more pronounced in OC compared to HSC due to the higher level of porosity (11.8%) in OC compared to HSC (8.8%), which explains the much lower strength of OC in saturated condition whereas both concretes present similar strengths in dry condition.

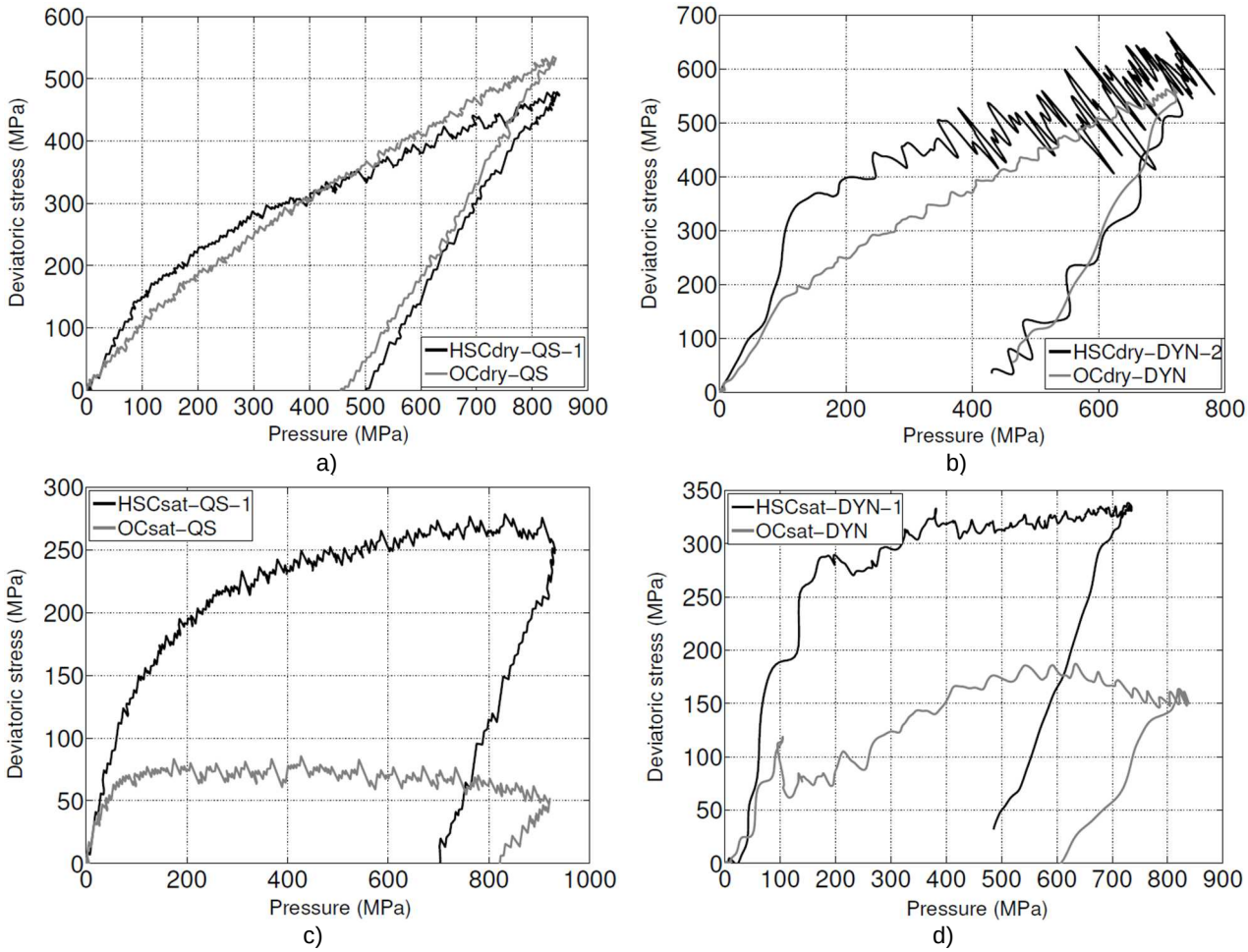

Figure 15.23 Quasi-oedometric compression tests applied to Ordinary Concrete (R30A7) and High-Strength Concrete in dry and saturated conditions [Piotrowska and Forquin, 2015]. (a) Quasi-static deviatoric behavior of dry OC and HSC concretes. (b) Dynamic deviatoric behavior of dry OC and HSC concretes. (c) Quasi-static deviatoric behavior of saturated OC and HSC concretes. (d) Dynamic deviatoric behavior of saturated OC and HSC concretes.

15.5.3 Influence of strain-rate and free-water on the confined shear strength of ordinary concrete

The shear strength of dry and wet ordinary concrete in static and dynamic conditions was explored by performing Oedo-PTS tests [Forquin, 2011; Forquin and Sallier, 2013] and PS-PTS tests [Abdulrahman et al, 2021]. The Figure 15.24 illustrates the influence of confinement stress and free water content on the shear strength of ordinary concrete in quasi static and dynamic loading conditions. On the one hand, at the same loading rate, it is clear that the shear strength increases with the confining level. For instance, In the case of wet concrete under dynamic test the shear stress increases from 32 MPa at a confinement stress of 10 MPa to 40 MPa at a confinement of 30 MPa. Higher confinement level was difficult to reach because concrete sample would have been damaged under compression during the pre-stressing stage (i.e. before applying the shear loading). In dry R30A7 a noticeable increase of shear strength is noted with the increase of confinement level. For instance, the dynamic shear strength increases from 30 MPa to 45 MPa with a confinement stress increasing from 15 MPa to 27MPa. An influence of strain-rate is also observed by comparing the static strength to the dynamic strength. For wet R30A7 concrete whereas the shear strength is around 20 MPa in static it is around 35 MPa in dynamic conditions at a confinement level of 15 MPa. Conversely, free water seems to have a little influence even if the shear strength of dry concrete looks a bit higher than that of wet concrete.

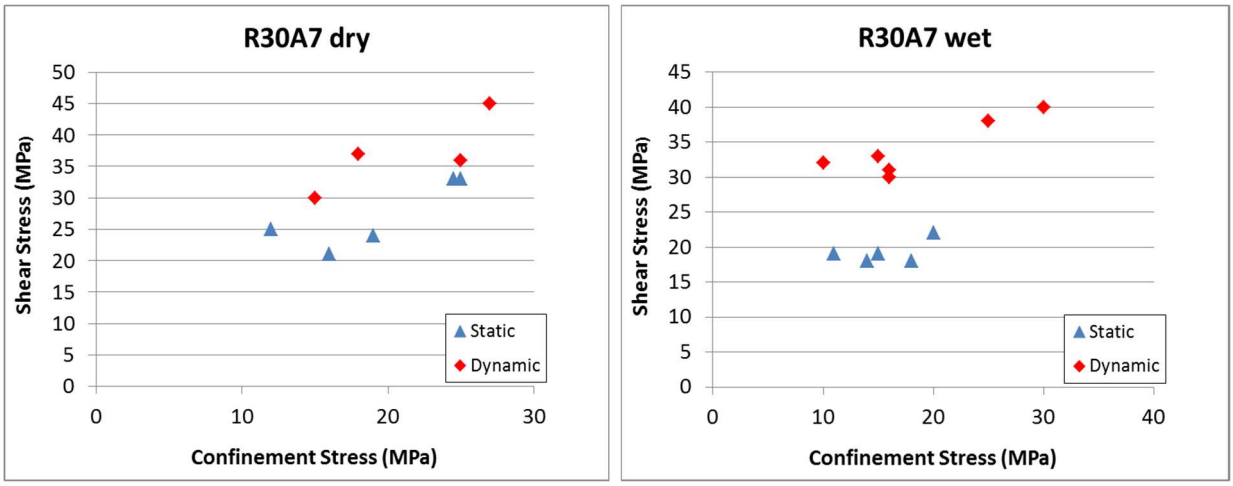

a) b)

Figure 15.24 Influence of confinement stress and free water content on the shear strength of ordinary concrete under quasi static and dynamic conditions. a) Dry concrete, (b) Wet concrete.

Influence of strain-rate, free water and aggregate size on the mechanical behavior of concrete when subjected to various loading conditions is summarized in Table 15.3. Influence of strain-rate is observed to be strong regarding the tensile strength of concrete, especially at strain-rates above a few $10s^{-1}$. Conversely, influence of strain-rate looks small or modest under confined shear and compression without, however, being able to be considered negligible. Free-water has very different effects depending on the loading conditions. Indeed, whereas free-water has a positive influence of tensile strength and seems to have a negative but weak influence on the concrete shear strength. Conversely, free-water has a major influence under confined compression, especially in dynamic conditions. Indeed, due to an increase of pore-pressure in water-saturated concrete, free-water leads to a strong thresholding effect on the deviatoric strength of concrete even if this phenomenon is partially compensated, at the same time, at the hydrostatic response is stiffened in wet concrete. On the other hand, aggregate size seems to be a less important parameter. In conclusion, strain-rate, free water content and confinement level appear as the most important parameters to be taken into account in any constitutive models used in computational codes to simulate the behavior of concrete structures subjected to intense dynamic loadings such as projectile impact or contact detonation.

Table 15.3 Relative influences of strain-rate, free water and aggregate size on the tensile, shear and confined behaviour of concrete.

Relative importance of:	Tensile strength in the range (1e-5 to 150 s^{-1})	Shear strength under low confinement	Deviatoric strength under high pressure	Hydrostatic behaviour under high pressure
Strain-rate	Strong increase	Little increase	Moderate increase	Little influence
Free-water	Positive but little	Little influence	Strongly negative (strength threshold)	Strongly positive (less compaction)
Aggregate size	Little influence	To be confirmed	Little influence	Little influence

15.5.4 Influence of the maximum aggregate size and sample size

Fig. 15.25a illustrates the influence of strain rate on the tensile strength of plain concrete, as measured on 60 mm cubic specimens composed of two different types of concrete with varying maximum aggregate sizes (5 and 10mm). It can be

concluded, based on the findings of Cadoni (2001), that at high strain rates, the uniaxial tensile strength of plain concrete tends to increase as the maximum size of aggregate particles decreases. This phenomenon can be explained by considering that reducing the maximum aggregate size leads to an increase in the surface area of the aggregate. Consequently, the likelihood of voids within the concrete decreases, thereby positively affecting the bond strength between the cement paste and aggregate particles. Furthermore, it has been observed that at high strain rates, the fracture occurs through the aggregates rather than around them. These factors justify the increase in uniaxial tensile strength of concrete with decreasing aggregate size, particularly in high-strain rate conditions ranging from 1 to 10 s^{-1}, where the influence of stress wave propagation is significant and the load increases rapidly. Upon examining the fracture surface of specimens tested at high strain rates, it becomes evident that numerous aggregates have participated in the fracture process. Size effects primarily arise from the inherent heterogeneity of the material, and they become more pronounced as the specimen dimensions increase. In other words, according to Weibull's model, larger specimens are more likely to contain elements with lower strength. Therefore, increasing the size of the specimen also increases the probability of observing a lower strength. Figure 15.26b presents the results of maximum tensile strength versus strain rate obtained from small (60 mm) and large (200 mm) cubic specimens composed of the same concrete with aggregate sizes of 10 mm.

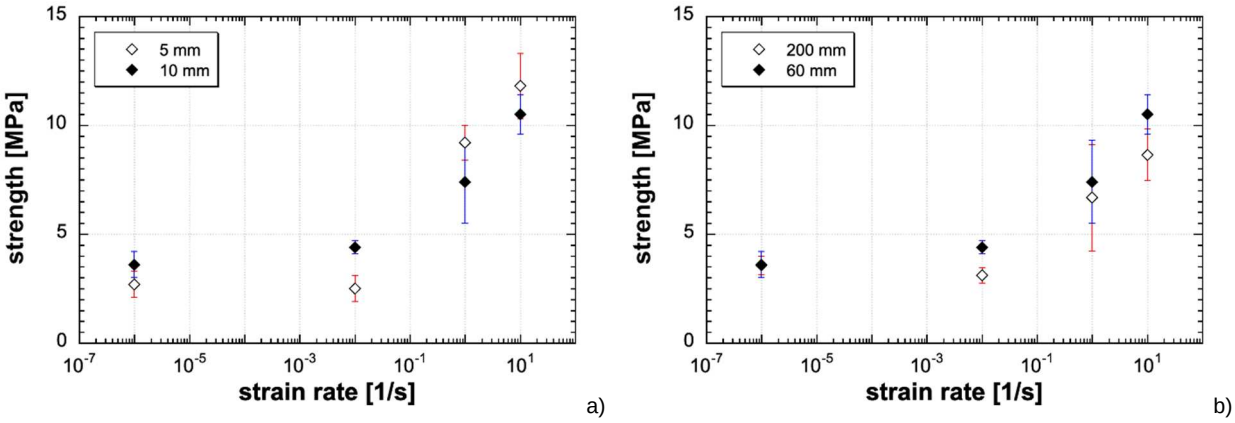

Figure 15.25 Influence of maximum aggregate size (a) and specimen size (b).

15.6 Ultra High Performance Concrete (with and without fiber)

The term Ultra-High Performance Fibre-Reinforced Concrete (UHPFRC) refers to a type of cementitious composite material. UHPFRC combines a cement-based matrix with reinforcing fibres and has a low water-to-cement ratio. As a result, it exhibits exceptional compressive strength (over 150 MPa), high durability, and improved aesthetic qualities. These remarkable characteristics have led to a constant increase in the global use of UHPFRC in construction. Initially, UHPFRC found applications in footbridges and pre-cast elements. However, its utilization has now expanded to include the rehabilitation and refurbishment of deteriorating concrete bridges, high-rise buildings, protective defense structures, offshore constructions, and façades. In UHPFRC, the volume fraction of fibres is significantly higher (around 2%) compared to ordinary fibre-reinforced concrete (FRC), which typically contains about 0.5% fibres per volume. This significant increase in fibre content in UHPFRC results in several interesting structural properties. The higher fibre reinforcement leads to improved tensile strength and ductility. Consequently, it becomes possible to replace some or all of the traditional reinforcement (rebar) typically used in reinforced concrete elements. Additionally, the inclusion of fibres enhances the energy absorption capacity of UHPFRC by allowing stress transfer even after the occurrence of initial cracking. As a result, UHPFRC exhibits a more favorable structural response to impact loading and reduces the risk of debris ejection caused by spalling in explosive situations.

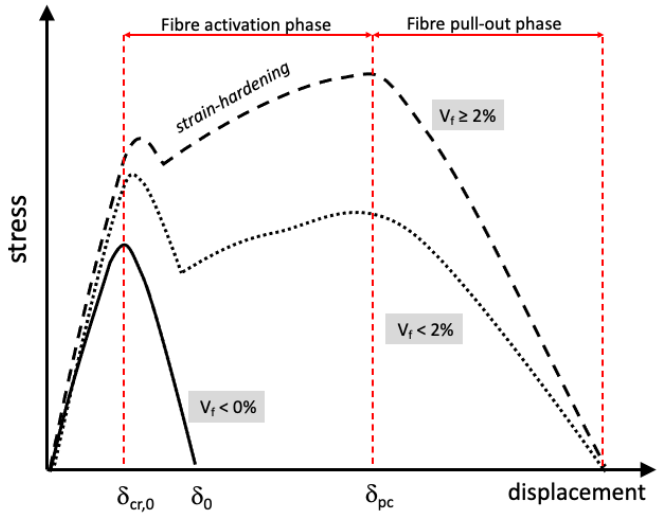

Figure 15.24 Behavior of the UHPFRC under tensile loading as a function of the fibre contents.

UHPFRC materials are commonly categorized based on their tensile behavior as either strain-softening or strain-hardening materials as shown in Fig. 15.24. In the case of strain-softening (fibre volume content V<2%), the contribution of fibres is primarily limited to transferring forces across cracks through fibre bridging, preventing brittle failure and leading to a gradual decrease in post-peak strength. In the case of strain-hardening (fibre volume content V>2%), UHPFRC exhibits the ability to further increase its tensile capacity due to multiple cracking phenomena and favorable fibre orientation, resulting in significant energy dissipation. The presence of a high fibre content can enhance the tensile strength beyond that of the matrix alone, but this is influenced by factors such as fibre shape, distribution, and orientation. It should be noted that the classification of UHPFRC as "softening" or "hardening" may not always apply universally, as it depends on various factors such as specimen size, shape, and fibre orientation. Therefore, this classification should be considered more as a structural characteristic rather than a fundamental material characteristic. The widespread adoption of UHPFRC is primarily driven by its exceptional mechanical properties, particularly its ability to dissipate a large amount of energy and its ultra-high strength. These characteristics make UHPFRC an excellent choice for protective structures. As a result, numerous research teams have begun proposing UHPFRC-based solutions for various types of loadings, including impact, blast, and close charge scenarios. These studies aim to enhance the design and application of UHPFRC in protective structures, ensuring their effectiveness and reliability. As a result of the fibres being included in UHPFRC, various mechanical properties improve, such as tensile strength, energy absorption, strain capacity, and elastic modulus. These properties improve as fibre volume increases.

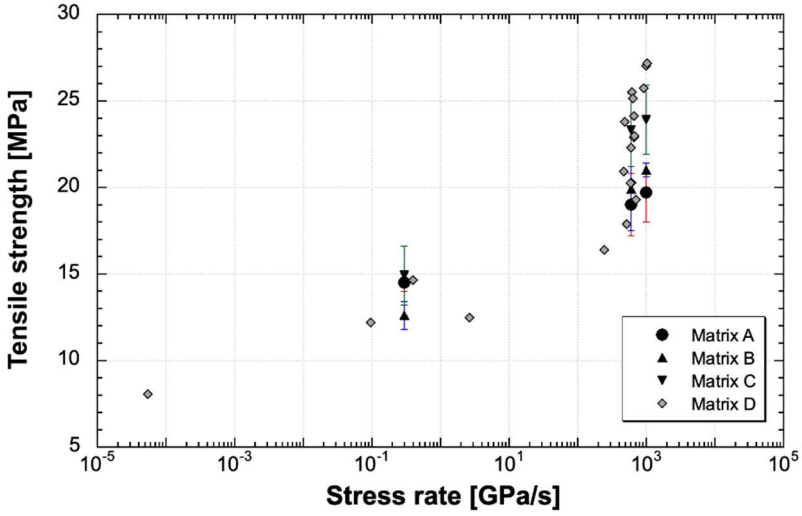

Figure 15.25 Tensile strength of the UHPFRC matrix versus stress rate.

Dynamic tensile behavior is highly sensitive to strain rate, particularly in the matrix (Fig. 15.25) [Cadoni et al. 2016, 2019]. The dynamic tensile strength increased with higher fibre volume content. Micro-straight steel fibres exhibited slightly better performance compared to the hooked ones. Moreover, the dynamic strength is positively influenced by an increase in fibre volume fraction, aspect ratio, and fibre length.

Synopsis

Concretes and cementitious materials may be among the most difficult materials to characterize in dynamic conditions due to their brittleness, their sensitivity to confining pressure, their heterogeneity within the microstructure (micro-pores, aggregates, cracks), and their sensitivity to environmental conditions (aging, temperature, free water content).Their dynamic mechanical properties are affected by strain-rate, pressure level, free water content, fibre content and orientation (when fibre-reinforced) and aggregate size. In the past few decades, new experimental methods and data processing technologies have been developed to analyse the tensile behaviour at different loading rates. There are limitations and drawbacks to each method, as well as applications that can be derived from them. High-speed hydraulic machines and Split-Hopkinson Bar apparatus are commonly used for medium strain rates (1e-3 s^{-1} to 10 s^{-1}), whereas spalling with a single Hopkinson bar is suitable for higher strain rates (20 s^{-1} to 200 s^{-1}). A comprehensive review of literature and experimental techniques highlights the effects of strain rate and free water content on concrete tensile strength.Finally, the development of new classes of Ultra-High Performance Fibre-Reinforced Concrete has been the subject of numerous research programs, mostly focused on the analysis of the dynamic behaviour. Over a wide range of strain rates, dynamic tensile tests revealed a continuous increase in tensile strength with loading-rate. Many aspects of the dynamic response of these materials are still open and need further investigations.

References

Abdul Rahman R., Forquin P. (2023) An Experimental Method to Characterize the Shear Behaviour of Concrete Under High Confinement. Exp Mech. https://doi.org/10.1007/s11340-023-00948-9

Abdul-Rahman R., Saletti D., Forquin P. (2021) Experimental study of the static and dynamic behavior of pre-stressed concrete subjected to shear loading. Engineering Structures, 234, 111865.

Antoun T., Seaman L., Curran D.R., Kanel G.I. Razorenov S.V., Utkin A.V. (2002) Spall fracture, Ed. Springer, New York, ISBN 0-387-95500-3.

Backers T., Stephansson O., Rybacki E. (2002) Rock fracture toughness testing in Mode II—punch-through shear test. Int. J. Rock Mech. Min. Sci. 39:755-769

Blasone M., Forquin P. (2020) Numerical Design of Plate-Impact Testing method to Determine the Spall strength of an Ultra-High Performance Concrete. DYMAT Winter School 2020, in Les Houches School of Physics, France.

Blasone M., Saletti D., Baroth J., Forquin P., Bonnet E., Delaplace A. (2021) Ultra-high performance fibre-reinforced concrete under impact of an AP projectile: Parameter identification and numerical modelling using the DFHcoh-KST coupled model. Int. J. Impact Eng., 152, 103838, DOI: 10.1016/j.ijimpeng.2021.103838.

Burlion, N., Pijaudier-Cabot, G., Dahan, N. (2001) Experimental analysis of compaction of concrete and mortar. Int. J. for Numerical and Analytical Methods in Geomechanics 25, 1467-1486

Cadoni E., Albertini C. and Solomos G. (2006) Analysis of the concrete behaviour in tension at high strain-rate by a modified Hopkinson bar in support of impact resistant structural design. J. Phys. IV France 134, 647–652.

Cadoni E., Labibes K., Albertini C., Berra M. and Giangrasso M. (2001) Strain-rate effect on the tensile behaviour of concrete at different relative humidity levels. Materials and Structures/Matériaux et Constructions, 34, 21-26.

Cadoni, E., Labibes, K., Berra, M., Giangrasso, M. and Albertini, C. (2001), 'Influence of Aggregate Size on Strain-Rate Tensile Behavior of Concrete', *ACI Materials Journal* **98**, 220-223.

Cadoni E., Solomos, G. and Albertini, C. (2009), 'Mechanical characterisation of concrete in tension and compression at high strain rate using a modified Hopkinson bar', Magazine of Concrete Research, 61(3), 221-230.

Asprone D., Cadoni E. and Prota A. (2009), 'Experimental Analysis on Tensile Dynamic Behavior of Existing Concrete under High Strain Rates', ACI Structural Journal 106, 106--113.

Cadoni E., Solomos G. and Albertini C. (2013), 'Concrete behaviour in direct tension tests at high strain rates', Magazine of Concrete Research 65(11), 660-672.

Cadoni, E., Forni, D., Bonnet, E. and Dobrusky, S. (2019), 'Experimental study on direct tensile behaviour of UHPFRC under high strain-rates', *Construction and Building Materials* **218**, 667 - 680.

Cadoni, E. and Forni, D. (2016), 'Experimental analysis of the UHPFRCs behavior under tension at high stress rate', *The European Physical Journal Special Topics* **225**(2), 253-264.

Cotterll, A.H. (1964) The mechanical properties of matter. New York; John Wiley & Sons Inc.

Dargaud M., Forquin P. (2021). A Shockless Plate-Impact Spalling Technique Based on Wavy-Machined Flyer-Plates to Evaluate the Strain-Rate Sensitivity of Ceramic Tensile Strength, J. Dynamic Behavior Mat., DOI: 10.1007/s40870-021-00317-4.

Erzar B., Forquin P. (2010) An experimental method to determine the tensile strength of concrete at high rates of strain. Experimental Mechanics, 50(7), pp. 941-955.

Erzar B., Forquin P. (2011). Experiments and mesoscopic modelling of dynamic testing of concrete, Mechanics of Materials, 43 pp. 505–527.

Erzar B., Forquin P. (2014). Analysis and modelling of the cohesion strength of concrete at high strain-rates. Int. J. Solids Struct., 51(14): 2559-2574

P. Forquin, L. Sallier. (2013) A Testing Technique to Characterise the Shear Behaviour of Concrete at High Strain-Rates. In: Chalivendra V., Song B., Casem D. (eds) Dynamic Behavior of Materials, Volume 1. Conference Proceedings of the Society for Experimental Mechanics Series. Springer, New York, NY, DOI: 10.1007/978-1-4614-4238-7_68

Forquin P, Zinszner J-L. (2017). A pulse-shaping technique to investigate the behaviour of brittle materials subjected to plate-impact tests. Phil. Trans. R. Soc. A, 375: 20160333

Forquin P. (2011) Influence of strain-rate and confining pressure on the shear strength of concrete. in Dyanamic Behaviour of Materials, T. Proulx, Ed. New York, NY: Springer New York, pp. 29–35

Forquin P. (2016). Procédé et dispositif pour mesurer la résistance des materiaux solides par impact de plaques sans choc, October 11 2016. Patent UGA, INPI, N°1000369617

Forquin P., Abdul-Rahman R., Saletti D. (2022) A novel experimental method to characterize the shear strength of concrete based on pre-stressed samples. Strain, e12407. DOI: 10.1111/str.12407

Forquin P., Arias A., Zaera R. (2007) An experimental method of measuring the confined compression strength of geomaterials. Int. J. Solids Struct., 44 (13), pp. 4291-4317
Forquin P., Blasone M., Georges D., Dargaud M., Saletti D., Andò E. (2020) The Brittle's CODEX chair, DYMAT Winter School 2020, in Les Houches School of Physics, France.
Forquin P., Gary G., Gatuingt F. (2008) A testing technique for concrete under confinement at high rates of strain. Int. J. Impact Eng., 35 (6), pp. 425-446
Forquin P., Lukić B. (2018). On the processing of spalling experiments. Part I: Identification of the dynamic tensile strength of concrete. J. Dyn. Behavior Materials. 4(1): 34–55, DOI: 10.1007/s40870-017-0135-1
Forquin P., Safa K., Gary G. (2010) Influence of free water on the quasi-static and dynamic strength of concrete in confined compression tests. Cement Concrete Res., 40(2), pp. 321-333
Grote D. L., S. W. Park, M. Zhou (2001). Experimental characterization of the dynamic failure behavior of mortar under impact loading. J. Applied Physics, 89(4), 2115-2123.
Klepaczko J.R., Brara A. (2001) An experimental method for dynamic tensile testing of concrete by spalling. Int. J. Impact Eng., 25, 387-409.
Kolsky H. (1949) An investigation of mechanical properties of materials at very high rates of loading, Proceedings of the Physical Society London; B 62:676-700
Lukić B., Saletti D., Forquin P. (2018). On the processing of spalling experiments. Part II: Identification of Concrete Fracture Energy in Dynamic Tension. J. Dyn. Behavior Materials. 4(1):56–73, DOI: 0.1007/s40870-017-0138-y.
Luong M.P. (1990) Tensile and shear strenghts of concrete and rock. Eng. Fracture Mech., 35(1/2/3), pp.127–135
Millon, O., Nöldgen, M., Thoma, K., Riedel, W., Fehling E. Fiber-reinforced ultra-high performance concrete under tensile loads, 9th Int Conf Mechanical and Physical Behaviour of Materials under Dynamic Loading - DYMAT 2009, 1 (2009) 671-677, DOI:10.1051/dymat/2009095
Novikov, S.A., Divnov, I.I., Ivanov, A.G. (1966) The study of fracture of steel, aluminium and copper under explosive loading, Fizika Metallov i Metallovedeniye 21 (4).
Pierron, F., Forquin, P. (2012) Ultra-High-Speed Full-Field Deformation Measurements on Concrete Spalling Specimens and Stiffness Identification with the Virtual Fields Method. Strain 48, 388–405. (doi:10.1111/j.1475-1305.2012.00835.x)
Piotrowska E., Forquin P., 2015. Experimental investigation of the confined behavior of dry and wet high-strength concrete: quasi static versus dynamic loading. J. Dynamic Behavior Mat. 1 (2), 191-200.
Rossi, P., van Mier, J.G.M., Boulay, C. and le Maou, F. (1992). The dynamic behaviour of concrete: influence of free water. Materials and Structures 25: 509-514
Schuler H., Mayrhofer C., Thoma K. Spall experiments for the measurement of the tensile strength and fracture energy at high strain rates, Int. Journal Impact Eng. 32 (2006); 1635-1650
Toulemonde F. (1994). Résistance au choc des structures en béton: Du comportement des matériaux au calcul des ouvrages. PhD thesis, Ecole Nationale des Ponts et Chaussées.
Vegt, I. and Weerheijm, J. (2019). Influence of moisture on the fracture behaviour of concrete loaded in dynamic tension. 9th International Conference on Fracture Mechanics of Concrete and Concrete Structures, FraMCoS-9
Vegt, I., Weerheijm, J. and Van Breugel, K. The fracture energy of concrete under impact tensile loading- a new experimental technique. CONSEC Conference (2007), Tours, France.
Watkins J. (1983) Fracture toughness test for soil-cement samples in mode II. Int. J. Fracture, 23, pp.135–138